Photothermal and host immune activated therapy of cutaneous tuberculosis using macrophage targeted mesoporous polydopamine nanoparticles

Shuhao Fan [a,b,1], Daina Zhao [a,b,1], Jiajun Wang [a,b,1], Yuhe Ma [a,b], Dongsheng Chen [a,b], Yuhe Huang [a,b], Tangxin Zhang [a,b], Yilin Liu [a,b], Jiaojiao Xia [c], Xueqin Huang [a,b], Yujia Lu [b], Yongdui Ruan [a], Jun-Fa Xu [a,b], Ling Shen [d,**], Fen Yang [a,b,***], Jiang Pi [a,b,*]

[a] Research Center of Nano Technology and Application Engineering, The First Dongguan Affiliated Hospital, School of Medical Technology, Guangdong Medical University, China
[b] Guangdong Provincial Key Laboratory of Medical Molecular Diagnostics, School of Medical Technology, Guangdong Medical University, Dongguan, China
[c] Department of Biochemistry and Molecular Biology, School of Basic Medical Sciences, Kunming Medical University, Kunming, China
[d] Department of Microbiology and Immunology, University of Illinois at Chicago, Chicago, IL, USA

ARTICLE INFO

ABSTRACT

Tuberculosis (TB) remains the leading cause of deaths among infectious diseases worldwide. Cutaneous Tuberculosis (CTB), caused by *Mycobacterium tuberculosis* (Mtb) infection in the skin, is still a harmful public health issue that requires more effective treatment strategy. Herein, we introduced mannose-modified mesoporous polydopamine nanosystems (Man-mPDA NPs) as the macrophage-targeted vectors to deliver anti-TB drug rifampicin and as photothermal agent to facilitate photothermal therapy (PTT) against Mtb infected macrophages for synergistic treatment of CTB. Based on the selective macrophage targeting effects, the proposed Rif@Man-mPDA NPs also showed excellent photothermal properties to develop Rif@Man-mPDA NPs-mediated PTT for intracellular Mtb killings in macrophages. Importantly, Rif@Man-mPDA NPs could inhibit the immune escape of Mtb by effectively chelating intracellular Fe^{2+} and inhibiting lipid peroxidation, and up-regulating GPX4 expression to inhibit ferroptosis of Mtb infected macrophages through activating Nrf2/HO-1 signaling. Moreover, Rif@Man-mPDA NPs-mediated PTT could effectively activate host cell immune responses by promoting autophagy of Mtb infected macrophages, which thus synergizes targeted drug delivery and ferroptosis inhibition for more effective intracellular Mtb clearance. This Rif@Man-mPDA NPs-mediated PTT strategy could also effectively inhibit the Mtb burdens and alleviate the pathological lesions induced by Mtb infection without significant systemic side effects in mouse CTB model. These results indicate that Rif@Man-mPDA NPs-mediated PTT can be served as a novel anti-TB strategy against CTB by synergizing macrophage targeted photothermal therapy and host immune defenses, thus holding promise for more effective treatment strategy development against CTB.

1. Introduction

Although many effective countermeasures have been implemented, tuberculosis (TB), caused by *Mycobacterium tuberculosis* (Mtb) infection, remains one of the most dangerous issues among infectious diseases worldwide. According to the WHO report in 2023, there are almost 10.6 million newly diagnosed active TB patients and 1.3 million deaths caused by TB worldwide [1]. Currently, the lungs are the most common site of Mtb infection, while 8 %–24 % of TB cases are extra-pulmonary, and cutaneous tuberculosis (CTB) accounts for about 1.5 %–3 % of these cases [1,2]. CTB is caused by Mtb infection in the skin by exogenous or endogenous route from infection foci within the organism itself. Skin

infections are easily overlooked as they present uncommonly and insidiously, often with multiple morphologies [3,4]. Currently, some effective anti-TB drugs, such as rifampicin (Rif), ethambutol, and isoniazide, have played a key role in the control of TB and CTB, either individually or in combination therapy. However, the low targeting effects of these anti-TB drugs result in the long treatment duration of CTB (6–18 months), with lots of unexpected issues including strong side effects and high incidences of drug-resistant mutants [5,6]. Thus, it's of vital importance to develop more effective anti-TB strategies with targeted drug killing features for CTB treatment.

Macrophages, as the key immune component of innate immunity and host cells against Mtb infection, can phagocytose and destroy different pathogens during infection, and initiate protective adaptive immune responses against infections via antigen presentation to T cells. However, Mtb has evolved very complicated strategies to evade the host immune anti-TB responses of different host cells, including macrophages. The immune escape mechanisms of Mtb, which include the inhibition of autophagy/apoptosis and the promotion of ferroptosis or necrosis of the Mtb infected macrophages, contribute to the survival of Mtb in macrophages and the further dissemination of Mtb to other sites [3,4,7,8]. Moreover, the immune escape of Mtb in macrophages also worses the killing efficiency of anti-TB drugs against intracellular Mtb, which would further worsen the treatment outcome of TB and CTB. Thus, there is an urgent need to develop novel anti-TB methods to inhibit the immune escape of Mtb, which would therefore benefit the more effective control of TB and CTB.

Phototherapy mainly includes photodynamic therapy (PDT) and photothermal therapy (PTT). In photodynamic therapy, under specific lighting conditions, photosensitizers can produce a large number of reactive oxygen species (ROS), which can kill tumor cells and mycobacterium tuberculosis [9,10]. Photothermal therapy (PTT) is currently attracting widespread attentions in antibacterial and anticancer therapy due to its non-invasive and deep tissue penetration [11–16]. With the development of nanotechnology, functional nanomaterials have been proved to show promising potentials for disease treatment [17–21], while some of them containing attractive photothermal effects can be further developed for advanced photothermal therapeutics [22]. Through certain modifications and particular concentration control of photosensitizers, PTT can be made to selectively act on the disease site with fewer side effects. For example, bionic erythrocyte membrane-treated nanoparticles have shown strong selective accumulation in TB granulomas to effectively kill Mtb in granulomas of pulmonary TB by PDT and PTT [23]. Photothermal effects generated by pre-activated macrophage membrane-coated nanoparticles are also proved to kill tuberculosis bacillus, reduce pathological damage and alleviate excessive inflammation in lungs of mice [24]. Although these results indicate attractive potentials of PTT for theranostic strategy development against pulmonary TB, there are still no previous works that applying PTT for CTB treatment. Moreover, these works keep the promise for anti-TB treatment by directly acting on the pathogen-Mtb by PTT, but how to applied PTT for more effective host directed therapy of TB by regulating the host anti-TB immunity remains a challenge.

PTT has been proven to promote protective autophagy in cells [25, 26], showing promising potential for host directed therapy against TB by activating host cell autophagy. Our previous results also indicated that functional nanoparticles could effectively activate host anti-TB immune responses and promote the efficiency of anti-TB drugs for more effective anti-TB treatment [27,28]. In addition, we also previously reported the use of mesoporous dopamine nanoparticles (mPDA NPs)-mediated PTT for synergistic cancer treatment by activating autophagy [11]. These attractive features enable functional nanomaterials to combine macrophage targeted drug delivery, PTT, and host anti-TB immune response regulations, thus providing new possibilities for the development of novel anti-TB and CTB therapeutics [24,29–31].

In this work, combining our decades-long expertise in tuberculosis immunology [32–35] and the advantages of nanobiotechnology [11,27,

36–39], we developed a kind of macrophage targeted mesoporous dopamine nanoparticles (Man-mPDA NPs) as rifampicin delivery system, aiming to combine the macrophage targeted drug delivery, PTT and host anti-TB immune responses for more effective treatment of CTB. The proposed rifampicin loaded Rif@Man-mPDA NPs could synergistically enhance intracellular Mtb killing efficiency in Mtb infected macrophages and effectively reduce Mtb burden in a mice CTB model, which may be served as more effective therapeutics against CTB.

2. Experimental section

2.1. Materials

7H9 medium, 7H11 medium and OADC were ordered from BD (USA). rhodamine123, Dialysis bags (MWCO: 8000–14,000), 1640 medium, protein assay kit, EDTA-trypsin, SDS, 4 % paraformaldehyde and penicillin/streptomycin were purchased from Solaibao (Beijing, China). Protein lysis buffer, nitrite assay kit, GAPDH antibody and anti-rabbit IgG were obtained from. Lyso-Tracker Red kit, Pluronic F-127 and DAPI were ordered from Sigma-Aldrich (USA). Other regents were listed as follows: FBS (zeta, USA), Bac Titer-Glo® reagent (Promega, USA), Annexin V-FITC/PI apoptosis detection kit (Multisciences, China), 2,7-dichlorodihydrofluoresce-in diacetate (DCFDA; MCE, USA). Dopamine hydrochloride (Macklin, China), 1,3,5-Trimethylbenzene (alanine, China).

2.2. Preparation and characterization of mPDA NPs, Man-mPDA NPs and Rif@Man-mPDA NPs

Firstly, F127 (0.1 g), dopamine hydrochloride (0.15 g) and TMB (0.16 mL) were dissolved in 10 mL of water/ethanol solution (1:1) by ultrasonication for 10 min to form emulsion solution. Then, 0.375 mL of ammonia was added dropwise to the above mixture for 2 h stirring, and the obtained particles were centrifugated at 12000 rpm for 10 min. Finally, the template was removed by ethanol and water to obtain the porous polydopamine nanoparticles. To synthesize Mannose-modified mPDA NPs (Man-mPDA NPs), 20 μL D-mannose (100 mM) dissolved in sodium acetate buffer (pH 4.0; 0.1 M) were added to 10 mL mPDA NPs (0.2 mg/mL) for 24 h incubation. Man-mPDA NPs were obtained by centrifugation, washed with PBS to remove unloaded mannose. Finally, 0.5 mg Man-mPDA NPs were dispersed into 1 mL rifampicin solution (0.2 mg/mL) for overnight incubation, Rif@Man-mPDA NPs were obtained by centrifugation, washed with PBS to remove unloaded rifampicin, and finally suspended in water for further use. The obtained nanosystems were characterized by dynamic laser light scattering (DLS, Horiba, Japan), transmission electron microscope (TEM, JEM, Japan) and fourier transform infrared spectroscopy (FTIR, Thermo Fisher Scientific, USA). The loaded rifampicin contents were analyzed by high performance liquid chromatography (HPLC, Shimadzu, Japan) using a Luna C18 column (250 mm × 4.6 mm × 5 μm) with wavelength set at 327 nm. Brunauer Emmett-Teller (BET) and Density Function Theory (DFT) were analyzed by using the United States Quantachrome Autosorb IQ3 model of 3-station automatic surface area analyzer, under the condition of 77k liquid nitrogen, the sample was tested for nitrogen absorption and desorption, and the isothermal absorption and desorption curve was obtained after the instrument analysis was completed. The total specific surface area of the material was obtained by BET method. The pore size and pore volume were analyzed by DFT.

2.3. Photothermal property analysis

The photothermal property was investigated by recording the temperature changes of sample under laser irradiation. Briefly, eppendorf tube with the mPDA NPs , Rif@Man-mPDA NPs or PBS solution were treated with laser irradiation at 808 nm (1.2 w/cm^2) for 5 min. The laser was adjusted to ensure that the irradiation point could cover the whole

surface of the samples, and the temperature was recorded using an infrared camera (FLIR ONE Pro, USA). To further evaluate the photo-stability and photocontrol of the mPDA NPs, the samples were irradiated with an 808 nm laser and the laser was cycled on/off three times, and the temperature changes were recorded using an infrared camera (FLIR ONE Pro, USA).

2.4. Bacteria and cell culture

The attenuated Mtb strain H37Ra was a generous gift from Prof. Guangxian Xu (Guangdong Medical University), and were cultured in 7H9 medium with 10 % OADC enrichment. THP-1 cells were obtained from ATCC (USA) and cultured with 1640 medium supplemented with 10 % FBS in a humidified atmosphere of 5 % CO_2 at 37 °C.

2.5. Cellular viability

THP-1 cells were seeded into 48 well plates (2×10^5/per well) with 100 nM PMA stimulation for 24 h incubation. 200 μL of medium was replaced with 10 % FBS containing equal volume of PBS or Rif@Man-mPDA NPs. The material content of each group was 10 μg/mL, 20 μg/mL, 50 μg/mL, 100 μg/mL, respectively. After 24 h of incubation, the number of living cells was detected by CCK-8 kit (Zeta life, USA). In consideration of the PTT efficacy, THP-1 cells were seeded into 48 well plates (2×10^5/per well) with 100 nM PMA stimulation for 24 h incubation. 200 μL of medium was replaced with 10 % FBS containing equal volume of PBS or Rif@Man-mPDA NPs. The material content of each group was 10 μg/mL, 20 μg/mL, 50 μg/mL, 100 μg/mL, respectively. After 4 h incubation, the cells were irradiated with a 1.2 w/cm², 808 nm laser for 5 min. After another 20 h incubation, the viability of cells was detected by using a CCK-8 assay.

2.6. Ex vivo cellular uptake of Rif@Man-mPDA NPs by T-cells, B-cells, and macrophages in mouse splenic lymphocytes

To determine the cellular uptake behaviour of macrophages for the Rif@Man-mPDA NPs system, Fluorescein Isothiocyanate (FITC) was encapsulated in the cavity of Man-mPDA NPs. Purified mouse splenic lymphocytes were seeded into 24-well plates (1×10^7 cells/well). Then, 5 μg/mL of FITC@Man-mPDA NPs or FITC@mPDA NPs were added to the cells and incubated for 1, 3 and 6 h. Cells were then collected, washed with PBS containing 2 % FBS and 2 mM EDTA (ethyl-enediaminetetraacetic acid), and then stained with PerCP anti-mouse CD14 antibody (Biolegend, USA), APC anti-mouse CD3e antibody (Biolegend, USA) and PE anti-mouse CD19 antibody (Biolegend, USA) for 30 min at 4 °C. After rinsing with PBS containing 2 % FBS and 2 mM EDTA, cellular uptake by T cells, B cells, and macrophages was analyzed by flow cytometry (BD, USA).

2.7. Cellular uptake and intracellular localization

THP-1 cells were seeded into 48 well plates (2×10^5 cells/well) with 100 nM PMA stimulation for 24 h incubation. The cells were then placed in medium containing FITC@Man-mPDA NPs and FITC@mPDA NPs. After incubation for 1, 3, 6 h, the cells were collected and washed with PBS. The fluorescence histograms of FITC were analyzed by flow cytometry (BD, USA). To evaluate the localization of Man-mPDA NPs in macrophages, THP-1 cells were seeded into glass-bottom confocal dish (1×10^5 cells/well) with 100 nM PMA stimulation for 24 h incubation. Then the cells were incubated in FITC@Man-mPDA NPs and FITC@mPDA NPs for 1, 3 and 6 h and then washed three times with PBS, and then stained with DID for cell membranes (10–15 min), Hochest for nuclei (30 min) and LysoTracker for lysosomes (30–60 min). The cells were washed with PBS for three times, and fixed with 4 % para-formaldehyde for 10 min. Images were captured by a Leica SP8 confocal microscope at different layers (Leica Microsystems, Wetzlar, Germany).

2.8. Cellular uptake mechanism of Rif@Man-mPDA NPs

The cellular uptake mechanism of Man-mPDA NPs in THP-1 cells was determined under different endocytosis inhibition conditions. The cells were seeded into 48 well plates (2×10^5 cells/well) with 100 nM PMA stimulation for 24 h, and then pre-treated with different inhibitors for 1 h (except that nystatin was pre-treated for 30 min). The concentration of specific endocytosis inhibitors were listed as following: sucrose (0.45 M), dynasore (80 μM), nystatin (10 μg/mL). Cells were then further incubated with 10 μg/mL FITC@Man-mPDA NPs for 3 h. The control cells were incubated with 10 μg/mL FITC@Man-mPDA NPs without the addition of inhibitors. For investigation of energy-dependent pathways, the cells were treated in complete medium at 4 °C for 4 h, followed by 10 μg/mL of FITC@Man-mPDA NPs incubation. For free mannose competition assay, different concentrations of mannose were added to the cells for 1 h incubation. The cells were then incubated with 10 μg/mL of FITC@Man-mPDA NPs for 3 h. After that, cells were washed with PBS and lysed by 0.5 % Triton X-100 in 0.2 M NaOH solution. Fluorescence microplate reader was used to measure the fluorescence intensity from nanoparticles inside the wells (excitation and emission wavelengths set at 485 and 528 nm, respectively). The cellular uptake efficacy was expressed as the percentage of the fluorescence of the testing wells over that of the control wells.

2.9. Fe²⁺-chelating capacity of Rif@Man-mPDA NPs

The concentration of Fe^{2+} was monitored using 1, 10 phenanthroline based strategy. Briefly, 100 μM $FeCl_2$ was incubated with Rif@Man-mPDA NPs at concentrations of 10, 20, 30, 50, 100, and 200 μg/mL for 1 h at room temperature. After centrifugation at 12000 rpm for 15 min, the concentrations of Fe^{2+} in supernatant were calculated by testing the absorbance of 1, 10-phenanthroline-Fe^{2+} at 510 nm using a microplate reader (TECAN, Switzerland). To determine the Fe^{2+}-chelating capacity of Rif@Man-mPDA NPs by zeta potential assay, 200 μg/mL Rif@Man-mPDA NPs solution was mixed with 0, 125, 250, 500, 1000 and 2000 μM of Fe^{2+} for 4 h incubation at room temperature. After that, Rif@Man-mPDA NPs were collected by 12000 rpm centrifugation for 15 min and washed several times with distilled water to remove the residual Fe^{2+}. Then, the zeta potential of nanoparticles dissolved in deionized water was determined by dynamic laser light scattering (DLS, Horiba, Japan).

2.10. Effects of Rif@Man-mPDA NPs on intracellular Fe²⁺ and lipid peroxidation

THP-1 cells were seeded into 48 well plates (2×10^5 cells/well) with 100 nM PMA stimulation for 24 h incubation. Then, the cells were infected with H37Ra using a multiplicity of infection (MOI) of 1 for 24 h. After washed with PBS to clean the H37Ra outside the cells, 10 μg/mL of Rif@Man-mPDA NPs, 1.3 ng/mL of rifampicin were added into the cells, after 4 h incubation, the cells were irradiated with a 1.2 w/cm², 808 nm NIR laser for 5 min and further cultured for 24 h. To determine intracellular Fe^{2+} levels, the cell culture medium was replaced with RIPM-1640 containing 1 μM FerroOrange (dojindo, Japan), and the cells were incubated for 30 min. The fluorescence histograms of FerroOrange were analyzed by flow cytometry (BD, USA). To visualize lipid peroxidation, the cells were incubated with 2.5 μM C11 BODIPY (dojindo, Japan) for 30 min, and the fluorescence histograms of C11 BODIPY were analyzed by flow cytometry (BD, USA).

2.11. Western blot analysis

THP-1 cells were seeded into 48well plates (2×10^5 cell/well) with 100 nM PMA stimulation for 24 h incubation, and then infected with H37Ra using a MOI of 1 for 24 h. After washed with PBS to clean the H37Ra outside the cells, 10 μg/mL of Rif@Man-mPDA NPs, 1.3 ng/mL of

rifampicin were added into the cells, after 4 h incubation, the cells were irradiated with a 1.2 w/cm², 808 nm NIR laser for 5 min and then cultured for 24 h or 72 h. THP-1 macrophages cells were incubated with lysis buffer containing protease inhibitors to obtain total cellular proteins. The protein concentration in the lysate was measured using the BCA protein assay kit. Proteins were then denatured by boiling at 100 °C for 10 min in sample buffer. The protein samples were then separated by electrophoresis on 10 % SDS-polyvinylamide minigels, and were then transferred to polyvinylidene difluoride membranes. The transferred membranes were blocked with 5 % skim milk in TBST solution for 1 h, and then washed three times with Tris-Buffered Saline and Tween 20 (TBST) (5 min each time). After incubated with primary antibodies, including LC3B antibody (Abcam, UK), GPX4 (Cell Signaling, USA), Nrf2 (Cell Signaling, USA), HO-1 (Cell Signaling, USA) or GAPDH antibody (Cell Signaling, USA) overnight at 4 °C, the membranes were washed three times with TBST, and incubated with secondary antibodies (Cell Signaling, USA) at room temperature for 1 h followed by wash with TBST (Tris Buffered Saline Tween) and ECL (Electrochemiluminescence) detection.

2.12. Direct inhibition effects of Rif@Man-mPDA NPs on extracellular Mtb

2×10^5 CFU of H37Ra suspension in 7H9 medium was added into a 2 mL tube incubate with different concentration of Rif@Man-mPDA NPs. After 4 h incubation, the bacteria were irradiated with a 1.2 w/cm², 808 nm NIR laser for 5 min, and were then further incubated for 72 h. After that, the H37Ra suspension from different groups were diluted by 7H9 medium, and the obtained dilutions were plated onto Middlebrook 7H11 plates. CFU counts on plates were measured at 3–4 weeks after the culture in an incubator.

2.13. Effects of Rif@Man-mPDA NPs on the growth of intracellular Mtb in THP-1 macrophages

THP-1 macrophages were seeded into 48 well plates (2×10^5 cell/well) with 100 nM PMA stimulation for 24 h incubation. Then, the cells were infected with H37Ra using a multiplicity of infection (MOI) of 1 for 24 h. After washed with PBS to clean the H37Ra outside the cells, 10 μg/mL of Rif@Man-mPDA NPs, 1.3 ng/mL of rifampicin were added into the cells for 4 h incubation. The cells were then irradiated with a 1.2 w/cm², 808 nm laser for 5 min and further cultured for 72 h. After that, 0.01 % SDS was used to lyse the cells for 15 min, and the cell lysis suspension was diluted into different concentration using 7H9 medium. The obtained dilutions were plated onto Middlebrook 7H11 plates, and the CFU counts on plates were measured after 3–4 weeks culture in incubator.

2.14. In vivo anti-TB effects of Rif@Man-mPDA NPs in Mtb infected CTB mice model

Animal experiments were approved by the Animal Ethics Committee of Guangdong Medical University with the approval number GDY2302471, and studies were performed following the approved guidelines and the ethics of Institutional Animal Ethics Committee. To test the *in vivo* anti-tuberculosis efficacy of Rif@Man-mPDA NPs, we established a Mtb-infected CTB mouse model. 8-week-old BALB/c mice were used for Mtb-infection after 2 weeks of accommodation in the labs, approximately 2×10^7 CFU of H37Ra resuspended in 50 μL saline were injected subcutaneously. After 7 days of infection, mice were distributed into 5 groups for subcutaneous administration: (1) control group (50 μL saline); (2) control group (50 μL saline), 1.2 w/cm², 808 nm laser irradiation for 5 min (3) rifampicin group (50 μL, 1.04 μg/kg); (4) Rif@Man-mPDA NPs group (50 μL, 8 mg/kg); (5) Rif@Man-mPDA NPs group (50 μL, 8 mg/kg) 1.2 w/cm², 808 nm laser irradiation for 5 min. Laser irradiation was performed 24 h after drug injection, and the affected areas of mice were recorded for 15 days. After 15 days, mice were scarified and their blood and organs were harvested. Skin cysts were homogenised and the lysate was spread on 7H11 agar plates for CFU counting for H37Ra. Skin cyst tissue, spleen, heart, liver and kidney were fixed and sectioned for H&E staining and microimaging of tissue structure. Skin cyst tissues were fixed with glutaraldehyde, then dehydrated, embedded, sectioned, and stained with hydrogen peroxide acetate, and then used for observation of mitochondrial status by TEM (Hitachi HT7800, Japan).

2.15. Statistical analysis

All experiments were conducted at least in triplicate, and all data are presented as mean ± S.D. Statistical significance was assessed by ANOVA and by independent *t*-test for pairwise comparison. $P < 0.05$ were considered as statistically significant.

3. Results and discussion

3.1. Preparation and characterization of Rif@Man-mPDA NPs

In the present study, mPDA NPs were synthesized using the same method as we previously reported [11]. Briefly, Pluronic F127 and TMB were used as the organic templates, while ethanol and ammonia were served as a co-solvent and catalyst for dopamine polymerization. The mesoporous structure was then fabricated by removing the templates to obtain mPDA NPs. Novelty, we further use mannose for the surface modification of mPDA NPs as mannose receptor is highly expressed in macrophages. The acid condition could result in the ring-opening of mannose to form an aldehyde group, which can react with the amino group of mPDA NPs to form Man-mPDA NPs. Rifampicin can then be encapsulated into Man-mPDA NPs to form Rif@Man-mPDA NPs (Fig. 1A).

As shown in Fig. 1B, TEM imaging of mPDA NPs revealed an average diameter of approximately 240 nm with a uniform spherical morphology. For Man-mPDA NPs, TEM imaging indicated larger average diameter of around 260 nm with the same morphology of mPDA NPs. After the loading of rifampicin, Rif@Man-mPDA NPs indicated an average diameter of about 280 nm by TEM imaging. The DLS results (Fig. 1C) also showed slight increase in the size of mPDA NPs after mannose modification and further rifampicin loading, consistent with the TEM results. However, the DLS results showed a larger diameter than TEM results, which might be attributed to the different processes involved in sample preparations. In the case of the TEM methods, TEM images depicts the actual size at the dried state of sample, whereas the size measured by the DLS method is a hydrodynamic diameter (hydrated state), which always shows a larger hydrodynamic volume of nanoparticles due to solvent effects in the hydrated state [40–43]. The surface zeta potential of the nanoparticles changed from −43.9 mV for mPDA NPs to −30.7 mV for Man-mPDA NPs and −36.6 mV for Rif@Man-mPDA NPs (Fig. 1D). The absolute values of the zeta potential were all larger than 30 mV (Fig. 1D), indicating the strong stability of these nanoparticles due to the electrostatic repulsion effects between them. Moreover, we also detected the particle size changes of Rif@Man-mPDA NPs within 15 days of storage at 4 °C and found no significant size changes of Rif@Man-mPDA NPs during the storage, which indicated the acceptable stability of Rif@Man-mPDA NPs for storage (Supplementary materials Fig. S1).

The loading contents of rifampicin in Rif@Man-mPDA NPs were determined by HPLC, which indicated that 1 mg of Rif@Man-mPDA NPs contained 0.13 μg of Rifampicin with a loading efficiency of 13 % [44]. (Fig. 1E). FTIR spectroscopy analysis (Fig. 1F-G) revealed that mPDA NPs showed absorption of benzene ring at 1620.149 cm⁻¹ and 1510.448 cm⁻¹, which could be attributed to the benzene structures of dopamine. Mannose showed typical FTIR telescopic and tensile vibration peaks of C-O group at 1641.04 cm⁻¹ and 1037.31 cm⁻¹. The modification of
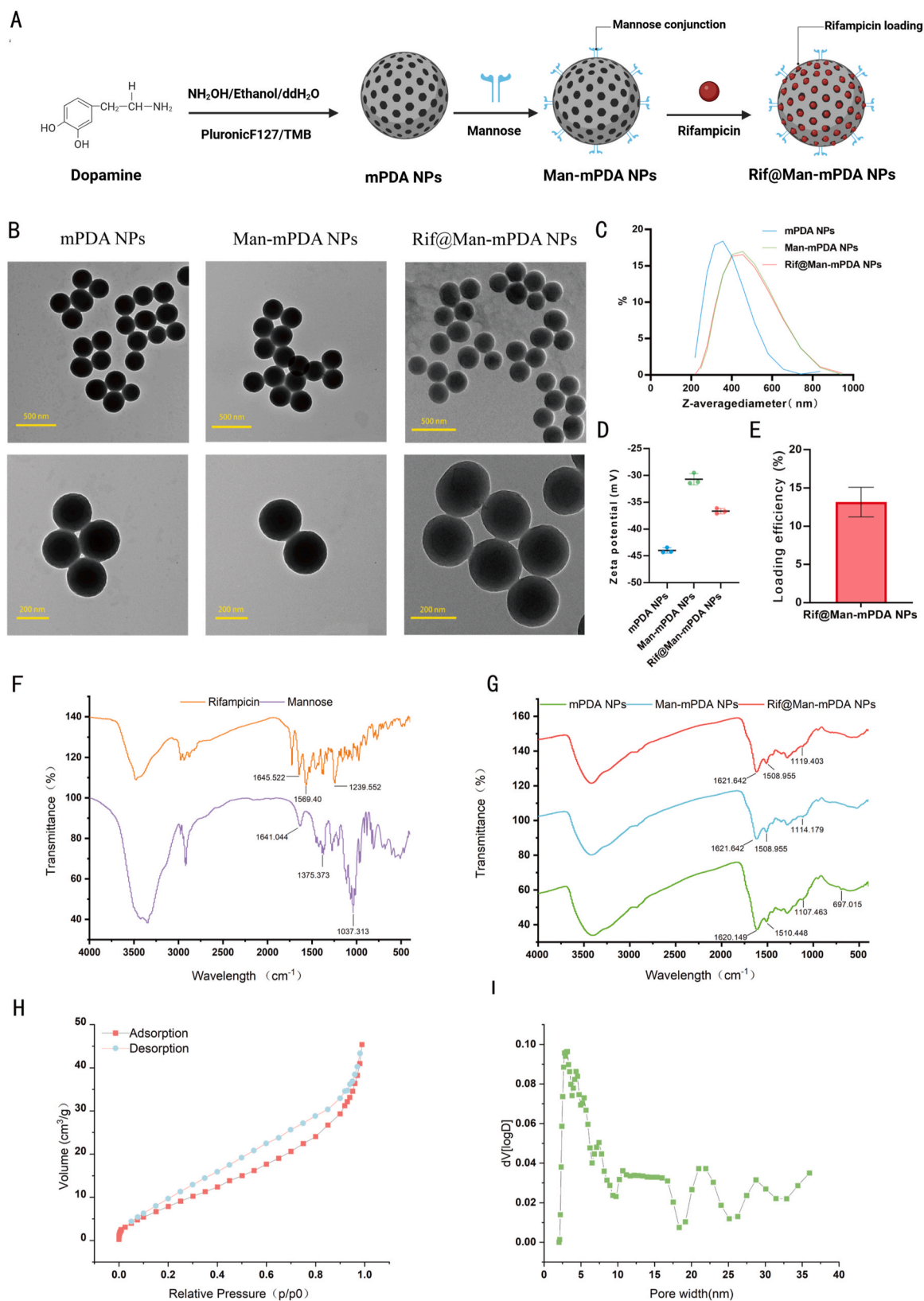
Fig. 1. Preparation and characterization of Rif@Man-mPDA NPs. (A) Schemes for the preparation of Man-mPDA NPs and Rif@Man-mPDA NPs (Figure was created with Biorender.com). (B) Transmission electron microscopy (TEM) imaging of mPDA NPs, Man-mPDA NPs and Rif@Man-mPDA NPs. (C) Hydrodynamic diameters of mPDA NPs, Man-mPDA NPs and Rif@Man-mPDA NPs by dynamic light scattering (DLS) analysis. Data are presented as means $\pm$ S. D, n = 3. (D) Zeta potentials of mPDA NPs, Man-mPDA NPs and Rif@Man-mPDA NPs by DLS analysis. (E) The loading efficiency of Rif@Man-mPDA NPs. (F–G) Fourier transform infrared spectroscopy (FTIR) analysis of mannose, rifampicin, mPDA NPs, Man-mPDA NPs and Rif@Man-mPDA NPs. (H) Nitrogen-adsorption-desorption isotherms of mPDA NPs. (I) Pore size distribution of mPDA NPs measured by Density functional theory (DFT) model.

mannose onto the mPDA NPs resulted in the red-shifting of the absorption peak of mPDA NPs from 1620.149 cm^{-1} to 1621.64 cm^{-1} due to the C-O groups on mannose, proving that mannose was modified onto the Man-mPDA NPs. Rifampicin showed a specific absorption peak at 1239.552 cm^{-1} on the -C-O-C moiety, which induced the red-shifted of the absorption peak at 1114.179 cm^{-1} for Man-mPDA NPs to 1119.403 cm^{-1}, after the loading of rifampicin onto the Rif@Man-mPDA NPs, which also proved the successful preparation of Rif@Man-mPDA NPs.

Moreover, we tested the N$_2$ adsorption-desorption isotherm curves of mPDA NPs to determine surface area and pore volume of the obtained mPDA NPs. As shown in Fig. 1H, the calculated BET surface areas of mPDA NPs and the DFT cumulative pore volumes were 38.451 m^2/g and 0.057 cm^3/g, respectively. And as shown in Fig. 1I, there were obvious mesopore structures ranging from 2.0 nm to 36 nm in the pore size distribution curve, with an average mesoporous size about 3.1 nm. These results collectively suggested the mesoporous structures of the obtained mPDA NPs.

mPDA NPs have been widely reported to show strong photothermal efficiency in ours and other's previous works [11,45]. Thus, we further investigated the photothermal properties of the Rif@Man-mPDA NPs system using NIR laser irradiation. The obtained results showed that Man-mPDA NPs and Rif@Man-mPDA NPs had similar warming curves, with rapidly increased temperatures within 5 min under NIR irradiation, reaching maximum temperatures of 48.4 °C and 51.3 °C, respectively (Fig. 2A and B). And under the same irradiation conditions, the temperature of PBS was almost unchanged (Fig. 2A and B), confirming the strong photothermal conversion properties of Man-mPDA NPs and

Rif@Man-mPDA NPs. These results indicated the excellent photothermal effects of mPDA NPs, and mannose modification did not weaken the photothermal efficiency of mPDA NPs. Thermal imaging showed a similar upward trend and high photothermal conversion capability of Rif@Man-mPDA NPs, which was crucial for their further PTT application. Rif@Man-mPDA NPs also showed concentration-dependent and power-density-dependent photothermal performance upon NIR irradiation (Fig. 2C and D). In addition, based on the heating-cooling curves (Fig. 2E), we found that Rif@Man-mPDA NPs exhibited almost the same photothermal interaction after 3 consecutive photothermal behaviors, which indicated the high photothermal stability of Rif@Man-mPDA NPs (Fig. 2F).

3.2. In vitro cellular uptake, intracellular localization and ex-vivo cellular uptake of Rif@Man-mPDA NPs

To apply Rif@Man-mPDA NPs-mediated PTT for anti-TB applications, we further evaluated the cytotoxicity of Rif@Man-mPDA NPs under different laser irradiation and concentration conditions. We found that the 808 nm NIR laser at 0.8 w/cm^2 and 1.2 w/cm^2 had fewer toxic effects on the cells, and Rif@Man-mPDA NPs-mediated PTT showed dose-dependent cytotoxicity in THP-1 macrophages (Fig. 3A). Based on these results, we then chosen 10 μg/mL of Rif@Man-mPDA NPs and 1.2 w/cm^2 of laser irradiation for the following PTT studies.

In order to validate the potential *in vivo* targeting effects of Rif@Man-mPDA NPs system, we investigated the uptake of FITC@Man-mPDA NPs by spleen lymphocytes from mice. As shown in Fig. 3B and the blank
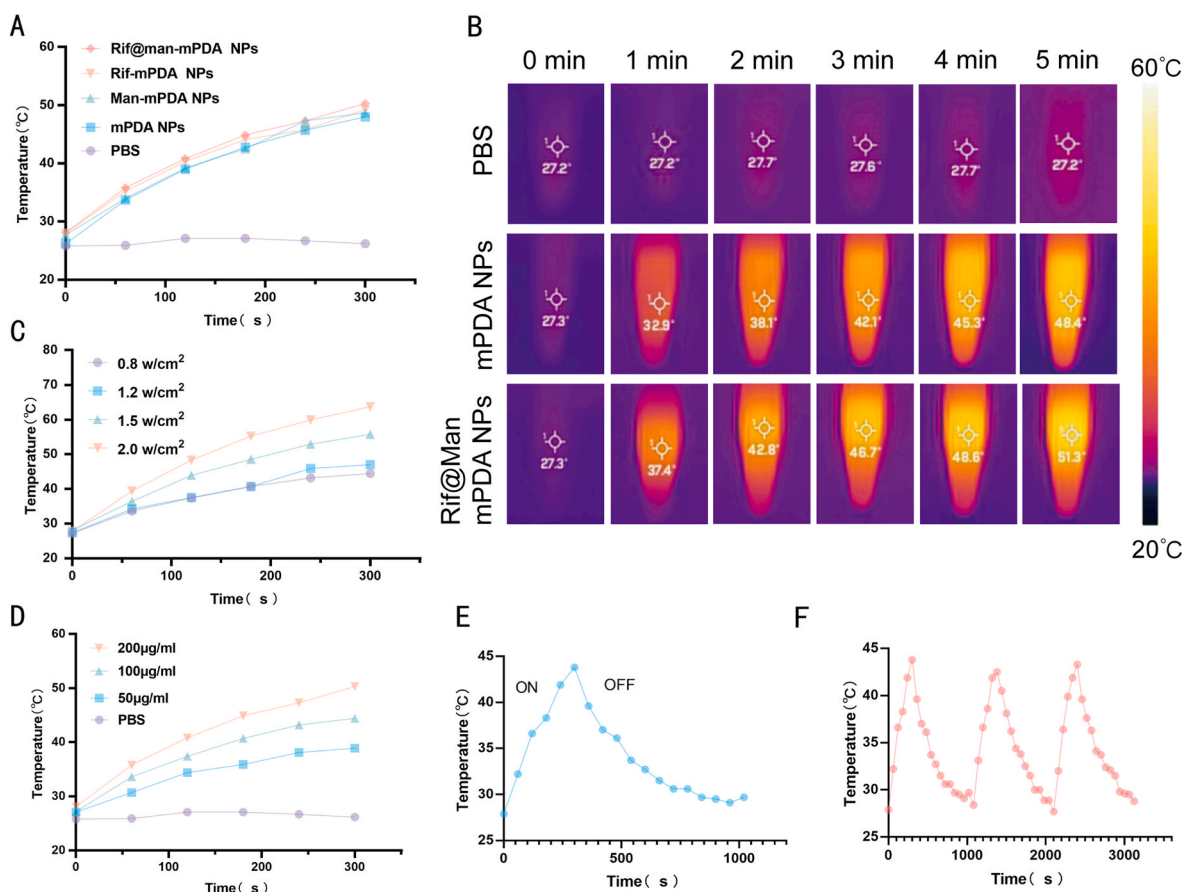

Fig. 2. Photothermal property characterization of Rif@Man-mPDA NPs. (A) Temperature profile and (B) thermographic images of PBS, mPDA NPs and Rif@Man-mPDA NPs solutions during NIR laser irradiation (808 nm, 1.2 w/cm^2, 5 min). (C) Temperature profile of Rif@Man-mPDA NPs during NIR laser irradiation with different power density (5 min).(D) Temperature profile of different Rif@Man-mPDA NPs concentrations during NIR laser irradiation (808 nm, 1.2 w/cm^2, 5 min). (E) Temperature profile of Rif@Man-mPDA NPs under NIR laser irradiation (808 nm, 1.2 w/cm^2, 5 min) and natural cooling. (F) Temperature changes of Rif@Man-mPDA NPs over three cycles of repeated NIR laser irradiation (808 nm, 0.8 w/cm^2, 5min/cycles).
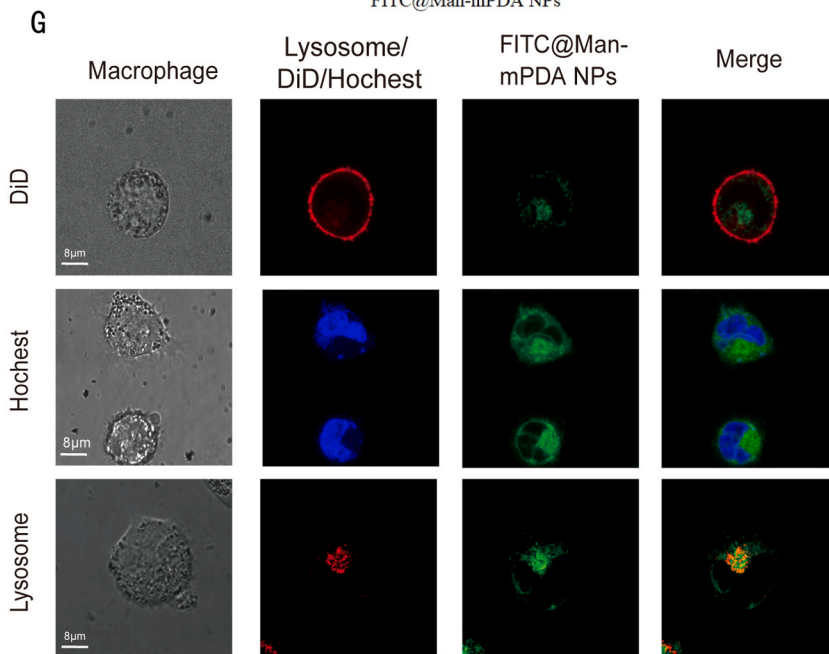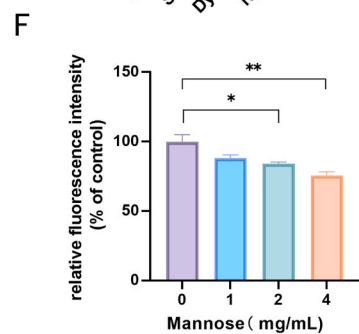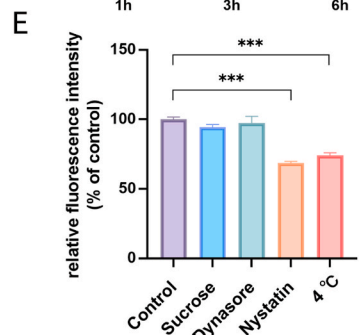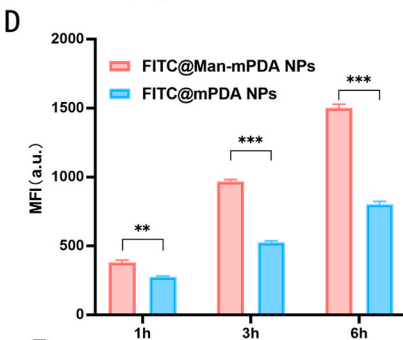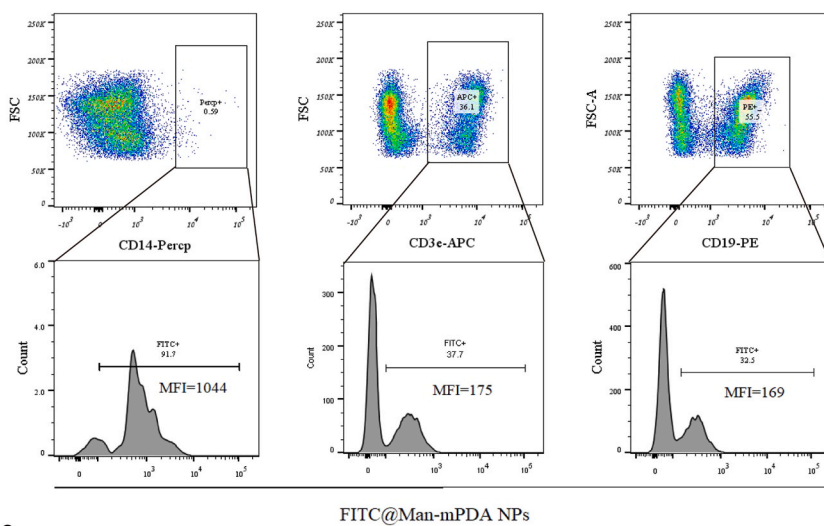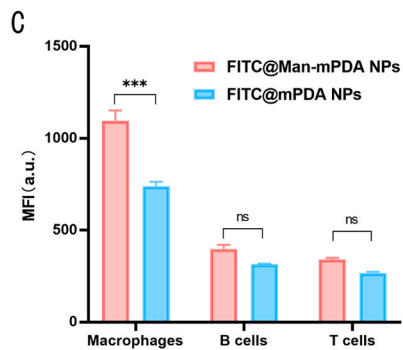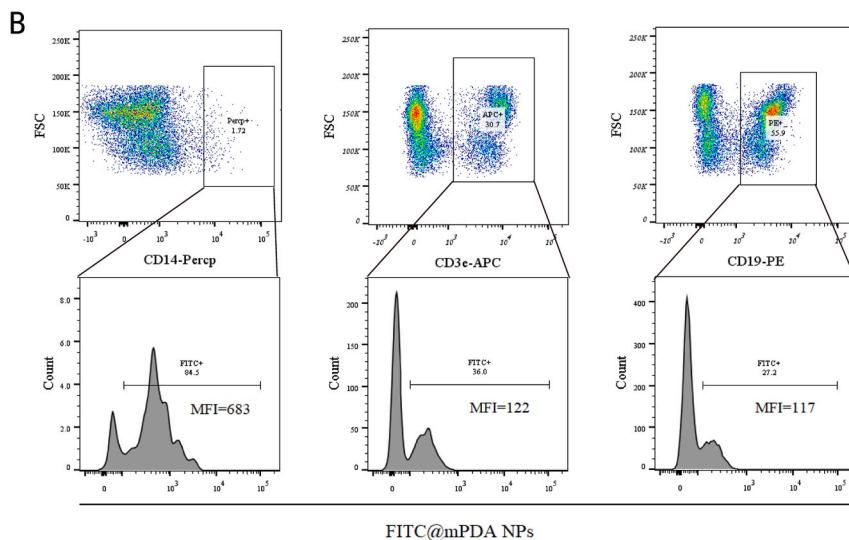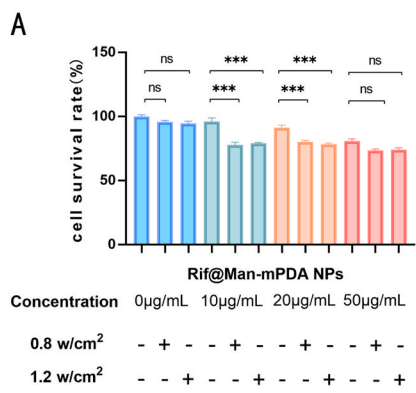
Fig. 3. Macrophage targeting effects and intracellular localization of Rif@Man-mPDA NPs. (A) Cytotoxicity of upon Rif@Man-mPDA NPs and laser treatment (808 nm, 0.8/1.2 w/cm^2, 5 min) in THP-1 macrophages. n = 3, *$p < 0.05$, **$p < 0.01$, ***$p < 0.001$. (B) Cellular uptake of FITC@Man-mPDA NPs by T-cells, B-cells and macrophages derived from mouse spleen after 3 h of treatment. (C) Statistical analysis for cellular uptake of FITC@Man-mPDA NPs by T-cells, B-cells and macrophages derived from mouse spleen after 3 h treatment, n = 3, *$p < 0.05$, **$p < 0.01$, ***$p < 0.001$. (D) Statistical analysis for cellular uptake of FITC@Man-mPDA NPs by THP-1 macrophages after 1, 3 and 6 h treatment, n = 3, *$p < 0.05$, **$p < 0.01$, ***$p < 0.001$. (E) Cellular uptake of FITC@Man-mPDA NPs by THP-1 macrophages under different endocytosis inhibition conditions, control group is treated without any inhibition conditions for FITC@Man-mPDA NPs uptake analysis, n = 3, *$p < 0.05$, **$p < 0.01$, ***$p < 0.001$. (F) Intracellular uptake of FITC@Man-mPDA NPs by THP-1 macrophages with free mannose competition, control group is treated without mannose for FITC@Man-mPDA NPs uptake analysis, n = 3, *$p < 0.05$, **$p < 0.01$, ***$p < 0.001$. (G) Fluorescence imaging for intracellular localization of FITC@Man-mPDA NPs with nucleus, cell membrane and lysosomes in THP-1 macrophages, scale bar: 8 μm.

control results in Supplementary materials Fig. S2, the *ex vivo* results indicated much higher uptake of FITC@Man-mPDA NPs by macrophages than that of T cells and B cells, which demonstrated the selective targeting effects of Rif@Man-mPDA NPs in primary macrophages. The statistical results (Fig. 3C) also demonstrated much higher uptake of FITC@Man-mPDA NPs by macrophages than that of T cells and B cells, and further indicated that the cellular uptake of FITC@Man-mPDA NPs by spleen macrophages was much higher than that of FITC@mPDA NPs. These results further indicated that mannose modification in Rif@Man-mPDA NPs could significantly enhance the macrophage targeting ability of the nanosystem.

The results above demonstrated that Rif@Man-mPDA NPs had selective targeting effects on macrophages (Fig. 3B), which highlighted their potential use in host cell directed TB therapies. Meanwhile, to further validate the verification that mannose surface modification could enhance the macrophage targeting of the nanosystems, we measured the fluorescence intensity by flow cytometer after incubating THP-1 macrophages with FITC@Man-mPDA NPs and FITC@mPDA NPs, and the results showed that the cellular uptake of FITC@Man-mPDA NPs by THP-1 macrophages was much higher than that of FITC@mPDA NPs (Fig. 3D and Supplementary materials Fig. S3). These results strongly demonstrated that mannose modification in Rif@Man-mPDA NPs could significantly enhance the macrophage targeting ability of the nanosystem.

To dissect the mechanisms for macrophage-targeted uptake of Rif@Man-mPDA NPs, THP-1 macrophages were pre-treated with different uptake inhibiting conditions before the addition of FITC@Man-mPDA NPs. The results suggested that the uptake of FITC@Man-mPDA NPs in macrophages was strongly inhibited by nystatin and low temperature, with uptake fractions reduced by about 40 % and 30 % compared to the control group (Fig. 3E). These results suggest that Rif@Man-mPDA NPs are mainly taken into macrophages by energetic as well as lipid raft-mediated endocytosis.

Next, to further explore the contribution of mannose receptor in the cellular uptake of Rif@Man-mPDA NPs in macrophages, macrophages were pre-treated with an excess amount of free mannose before the addition of FITC@Man-mPDA NPs. We found that free mannose significantly inhibited macrophage-targeted uptake of FITC@Man-mPDA NPs in a dose-dependent manner, with nearly 25 % of cellular uptake inhibition upon 4 mg/mL mannose pre-treatment (Fig. 3F). These results suggested that mannose receptor mediated endocytosis also significantly contributed to the selective targeting effects of Rif@Man-mPDA NPs in macrophages, which was consistent with the appealing hypothesis that mannose surface decoration could increase the macrophage targeting effects of Rif@Man-mPDA NPs.

The intracellular fate of nanomaterial-based drug delivery systems, such as their toxicity and drug release, is closely associated with their intracellular localization [46]. As macrophages are the major host cells for Mtb infection [47], we then preferred to explore the subcellular co-localization of Rif@Man-mPDA NPs in macrophages, which might play critical roles in the anti-TB activity of Rif@Man-mPDA NPs. Lysosomes have now been found to play vital roles in the intracellular transport and degradation of nanomedicines as the most important organelle for cellular degradation functions [29,48]. Our previous works also demonstrated that lysosomal targeting effects of nanosystem may introduce better drug release behaviors to enhance bactericidal function

[28]. Here, our fluorescence imaging showed that FITC@Man-mPDA NPs were able to cross the membrane, enter into the cytoplasm and then accumulate into the lysosomes to show bright and intense yellow fluorescence (Fig. 3G and Supplementary materials Fig. S4). These results indicated that lysosome was the main target organelle for Rif@Man-mPDA NPs in macrophages.

3.3. Rif@Man-mPDA NPs-mediated PTT inhibit ferroptosis by modulating Nrf2/HO-1 signaling pathway and enhance autophagy in Mtb-infected macrophages

Macrophages are the main host cells and the first-line of immunological defense against Mtb, thus playing critical roles in Mtb infections [3,49]. Host-pathogen interactions between macrophages and Mtb are a key component in the treatment of Mtb that needs further in-depth explorations. The battles between Mtb and macrophages are very complicated processes: the macrophages are trying to inhibit the Mtb replication and kill the Mtb inside themselves by several host immune mechanisms, while the Mtb do their best to escape from the immunological clearance of macrophages to replicate more for further dissemination by inhibiting the anti-TB immune mechanisms of macrophages. In Mtb infected macrophages, several cellular signaling events have been recognized as innate immune defense mechanisms for intracellular Mtb inhibition and clearance, such as the initiation of apoptosis and autophagy, and the inhibition of necrosis and ferroptosis [50,51]. However, virulent Mtb can release some toxic bacterial components to inhibit apoptosis and autophagy of the infected macrophages, while also promote the necrosis and ferroptosis of the infected macrophages, to escape from the immunological clearance of Mtb [50,52]. Thus, modulating macrophage immunological defense mechanisms is expected to be served as the most important host direct therapy strategy against TB and drug-resistant TB.

Mtb-infected macrophages are typically characterized by enhanced ferroptosis [53,54], which is associated with elevated intracellular Fe^{2+} levels triggering the Fenton reaction and inducing the production of large amounts of hydroxyl radicals. This process could sequentially impair glutathione peroxidase 4 (GPX4) activity and anti-lipid peroxidation ability, which ultimately leads to lipid peroxidation of phospholipids, cell disintegration, and death of infected macrophages for the survive and further dissemination of Mtb [8,55–57]. Previous studies have demonstrated that mPDA NPs exhibit Fe^{2+} chelation effects and thus influence ferroptosis in various cell types [58,59]. Therefore, we also investigated the effects of Rif@Man-mPDA NPs on Fe^{2+} in solution, which indicated that Rif@Man-mPDA NPs could effectively chelate Fe^{2+} in a dose dependent manner (Fig. 4A). Moreover, we further tested the zeta potential of Rif@Man-mPDA NPs after the incubation with different concentrations of Fe^{2+}. We could clearly found that the zeta potential of Rif@Man-mPDA NPs significantly changed from nearly −40 mV to −20 mV after 500 μM of Fe^{2+} incubation, and further changed to 20 mV after 2 mM of Fe^{2+} incubation (Fig. 4B). The changed zeta potential of Rif@Man-mPDA NPs upon Fe^{2+} incubation indicated that Rif@Man-mPDA NPs could effectively chelate Fe^{2+}, which thus show potentials to inhibit Fe^{2+} mediated ferroptosis in Mtb infected macrophages.

We then further examined the changes of Fe^{2+} contents in H37Ra-infected THP-1 macrophages with FerroOrange, which revealed that
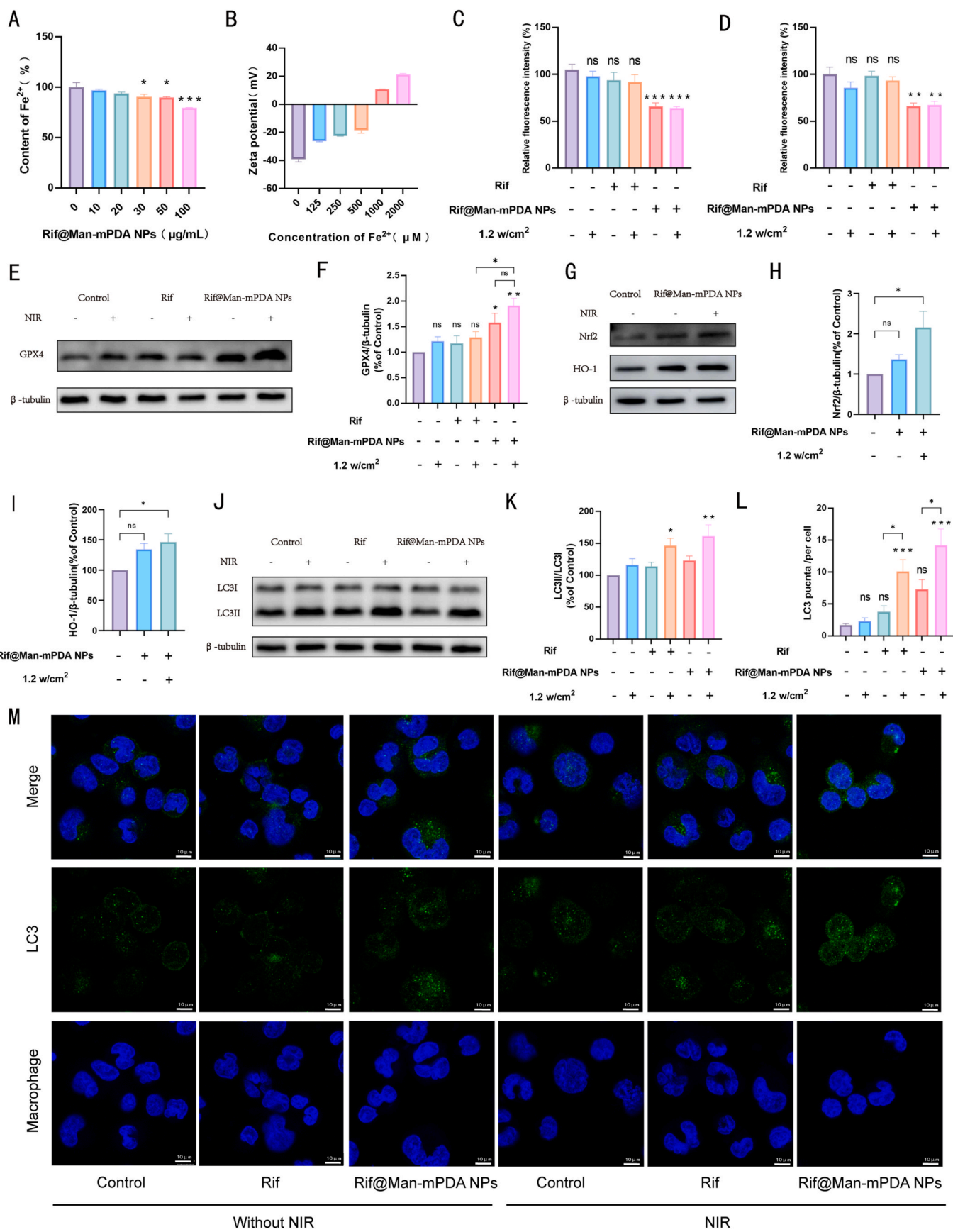
(caption on next page)

Fig. 4. Rif@Man-mPDA NPs inhibit ferroptosis and promote autophagy in Mtb-infected macrophages. (A) Fe^{2+} chelation efficiency of Rif@Man-mPDA NPs. n = 4 *p < 0.05, **p < 0.01, ***p < 0.001. (B) Zeta potential of Rif@Man-mPDA NPs after incubation with different concentrations of Fe^{2+}, n = 3. (C) Flow cytometry analysis of Fe^{2+} content in Mtb-infected THP-1 macrophages treated with Rif@Man-mPDA NPs and NIR irradiation (808 nm, 1.2 w/cm^2, 5 min). n = 9, *p < 0.05, **p < 0.01, ***p < 0.001. (D) Flow cytometry analysis of lipid peroxidation in Mtb-infected THP-1 macrophages treated with Rif@Man-mPDA NPs and NIR irradiation (808 nm, 1.2 w/cm^2, 5 min), n = 4, *p < 0.05, **p < 0.01, ***p < 0.001. (E) Immunoblotting of GPX4 in Mtb-infected THP-1 macrophages treated with Rif@Man-mPDA NPs and NIR irradiation (808 nm, 1.2 w/cm^2, 5 min) for 72 h. (F) Statistical results for GPX4 in Mtb-infected THP-1 macrophages before and after Rif@Man-mPDA NPs and NIR irradiation treatment (808 nm, 1.2 w/cm^2, 5 min) n ≥ 3, *p < 0.05, **p < 0.01, ***p < 0.001. (G) Immunoblotting of Nrf2 and HO-1 in Mtb-infected THP-1 macrophages treated with Rif@Man-mPDA NPs and NIR irradiation (808 nm, 1.2 w/cm^2, 5 min) for 24 h. (H–I) Statistical results for the Nrf2 and HO-1 in Mtb-infected THP-1 macrophages before and after Rif@Man-mPDA NPs and NIR irradiation (808 nm, 1.2 w/cm^2, 5 min) treatment. n ≥ 3,*p < 0.05, **p < 0.01, ***p < 0.001.(J) Immunoblotting of LC3B in Mtb-infected THP-1 macrophages treated with Rif@Man-mPDA NPs and NIR irradiation (808 nm, 1.2 w/cm^2, 5 min) for 24 h. (K) Statistical results for LC3B in Mtb-infected THP-1 macrophages before and after Rif@Man-mPDA NPs and NIR irradiation treatment (808 nm, 1.2 w/cm^2, 5 min) n ≥ 3,*p < 0.05, **p < 0.01, ***p < 0.001.(L) Statistical results of LC3B punctas for H37Ra infected THP-1 macrophages before and after Rif@Man-mPDA NPs and NIR irradiation treatment (808 nm, 1.2 w/cm^2, 5 min) n = 10,*p < 0.05, **p < 0.01, ***p < 0.001. (M) Typical fluorescence imaging of LC3B staining in H37Ra infected THP-1 macrophages before and after Rif@Man-mPDA NPs and NIR irradiation treatment (808 nm, 1.2 w/cm^2, 5 min)scale bar: 10 μm.

both Rif@Man-mPDA NPs and Rif@Man-mPDA NPs-mediated PTT could effectively chelate Fe^{2+} in Mtb infected macrophages (Fig. 4C and Supplementary materials Fig. S5). Additionally, we investigated whether Rif@Man-mPDA NPs could inhibit the lipid peroxidation in H37Ra infected THP-1 macrophages after chelating Fe^{2+}, which demonstrated that Rif@Man-mPDA NPs and Rif@Man-mPDA NPs-mediated PTT could effectively inhibit the degree of lipid peroxidation in Mtb infected macrophages (Fig. 4D and Supplementary materials Fig. S6). Furthermore, to elucidate the role of ferroptosis in Mtb-infected macrophages following Rif@Man-mPDA NPs treatment, we examined the protein expression level of GPX4 in H37Ra infected THP-1 macrophages, which was found to be significantly activated after Rif@Man-mPDA NPs and Rif@Man-mPDA NPs-mediated PTT treatment (Fig. 4E and F). We further examined the expression of Nrf2 and HO-1 and found that Rif@Man-mPDA NPs and Rif@Man-mPDA NPs-mediated PTT treatment could effectively increase Nrf2 and HO-1 expression (Fig. 4G–I). As Nrf2/HO-1 signaling axis has been proved to negatively regulate ferroptosis [60,61], our results indicated that Rif@Man-mPDA NPs-m ediated PTT treatment could effectively chelate intracellular Fe^{2+} to inhibit ferroptosis by regulating cellular iron accumulation and oxidative stress through the Nrf2/HO-1/GPX4 signaling axis.

Autophagy, a self-degradation process to remove of unnecessary functional or dysfunctional components through lysosome-dependent regulatory mechanisms, has been widely demonstrated to be an innate immune response for the inhibition and killing of intracellular pathogens [50,62]. The strategy of promoting autophagy to kill and inhibit intracellular Mtb has been widely proved by ours and other's previous works [27,63], demonstrating the promising potentials of autophagy regulations for anti-TB treatments. Nanomaterial-assisted PTT can induce hyperthermia of the treated cells, which would therefore trigger the protective autophagy of the cells to protect themselves from hyperthermia induced death [64]. Our previous work has also indicated the ability of mPDA NPs-mediated PTT to trigger the autophagy of cancer, which also indicated the potentials of Rif@Man-mPDA NPs-mediated PTT treatment to promote autophagy of Mtb infected macrophages. As shown in Fig. 4J and K, our results indicated that Rif@Man-mPDA NPs-mediated PTT treatment could significantly promote the autophagy of H37Ra infected THP-1 macrophages. It was worth to note that free rifampicin combined with PTT could also promote the autophagy of H37Ra infected THP-1 macrophages (Fig. 4J and K), which might also be attributed to PTT promoted protective autophagy. Confocal immunofluorescence staining results of LC3B in H37Ra infected THP-1 macrophages also indicated the increase of LC3B punctas (Fig. 4L and M), which collectively demonstrated that Rif@Man-mPDA NPs-mediated PTT could effectively promote the autophagy of Mtb infected macrophages. Moreover, it has been proved that the activation of Nrf2/HO-1 is also involved in the regulation of autophagy signalings [65]. We thus concluded that Rif@Man-mPDA NPs-mediated PTT could promote autophagy of Mtb infected macrophages by regulating the formation of autophagosomes through Nrf2/HO-1, but the exact mechanisms for this selectivity remained to be further investigated in the following work.

3.4. Rif@Man-mPDA NPs-mediated PTT significantly inhibit extracellular M.tb and intracellular M.tb in infected macrophages

Our above results have shown that the macrophage-targeted Rif@-Man-mPDA NPs can be used as a drug delivery system that can accumulate in the lysosomes of macrophages. Moreover, Rif@Man-mPDA NPs possess very good photothermal effects, and Rif@Man-mPDA NPs-mediated PTT could effectively inhibit immune escape mechanisms of Mtb, which is thus expected to achieve synergistic Mtb killing. To verify the Mtb killing effects of Rif@Man-mPDA NPs and further confirm whether Rif@Man-mPDA NPs could synergistically enhance Mtb clearance effects in Mtb-infected macrophages, we comparatively tested the killing efficiency of cultured extracellular Mtb and intracellular Mtb in macrophages.

In the culture test of extracellular Mtb, representative 7H11 plates for different groups and statistical results indicated that Rif@Man-mPDA NPs could significantly kill extracellular H37Ra, and its inhibittion function was further significantly enhanced under NIR laser irradiation (Fig. 5A and B). NIR irradiation further enhanced anti-TB efficiency of Rif@Man-mPDA NPs may be associated with the more complete release of rifampicin under laser irradiation for Mtb killings and the increased temperature to affect the integrity of the bacterial cell wall and membrane of Mtb [66,67]. These results indicated the strong potential of Rif@Man-mPDA NPs-mediated PTT for anti-TB treatments against intracellular Mtb and *in vivo* Mtb models.

Rifampicin is widely used as the first-line anti-TB drug in clinic. However, the efficacy of rifampicin is significantly hampered by its poor uptake by macrophages and macrophage-mediated drug efflux, hindering intracellular rifampicin levels [68]. Furthermore, we also tested the effects of Rif@Man-mPDA NPs on intracellular Mtb, which indicated that 10 μg/mL of Rif@Man-mPDA NPs could significantly inhibit intracellular H37Ra growth in THP-1 macrophages while the equivalent amount of free rifampicin showed much weaker inhibition effects (Fig. 5C and D). The higher intracellular Mtb inhibition effects of Rif@Man-mPDA NPs might be attributed to the enhanced cellular uptake of Rif@Man-mPDA NPs into macrophages and their sustained drug release for intracellular Mtb killings. The effects of Rif@Man-mPDA NPs to inhibit ferroptosis in Mtb infected macrophages also contributed to the enhanced intracellular Mtb killing effects of Rif@Man-mPDA NPs. Moreover, we found that NIR laser irradiation could further enhance the inhibition effects of Rif@Man-mPDA NPs on intracellular H37Ra in THP-1 macrophages, while the laser irradiation alone didn't show similar significant inhibition effects (Fig. 5C and D). These enhanced intracellular Mtb killing effects of Rif@Man-mPDA NPs-mediated PTT could be mainly attributed to the enhanced autophagy induction of Mtb infected macrophages, which has been highlighted as one of the most critical host immunological defense mechanisms of macrophage for intracellular Mtb clearance [69].
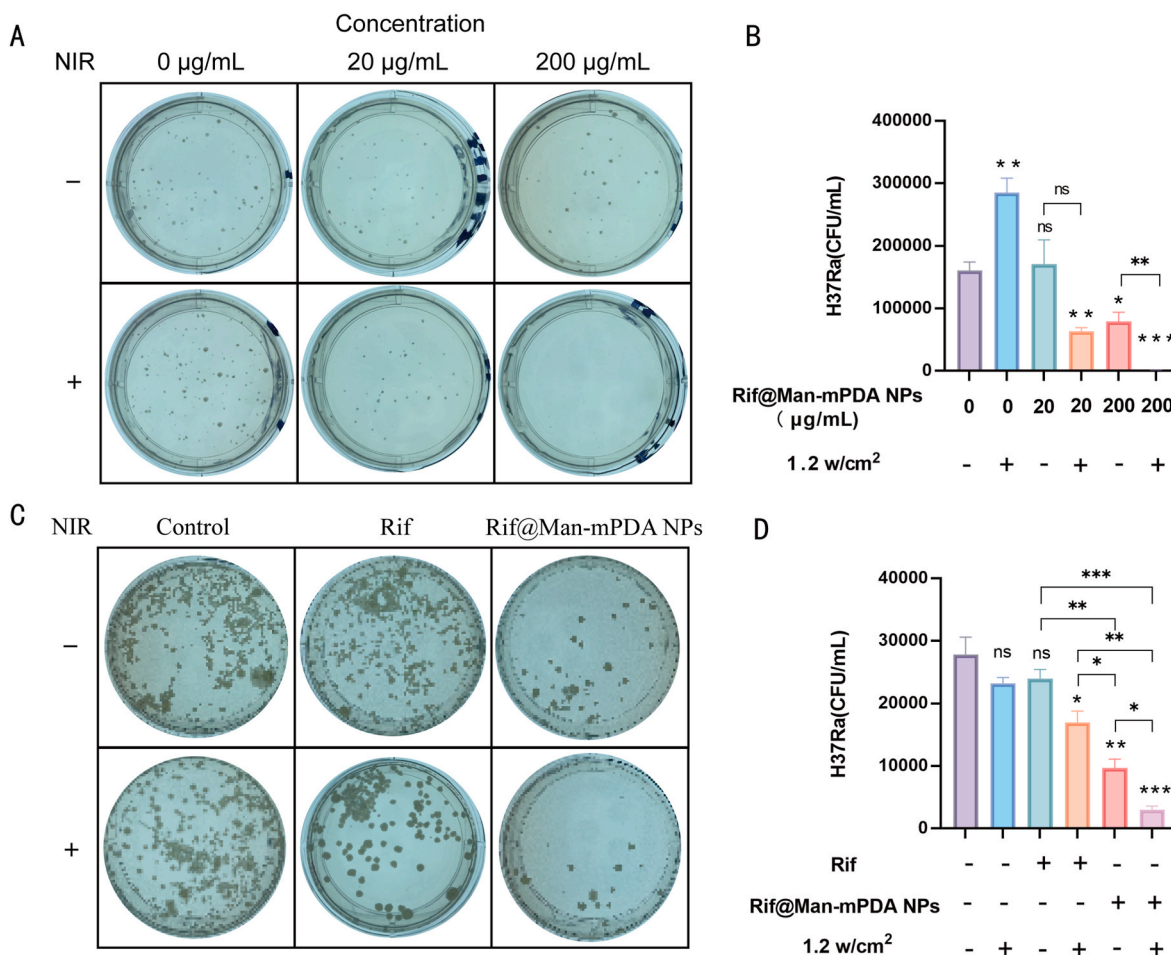
Fig. 5. Ex vivo anti-TB effects of Rif@Man-mPDA NPs-mediated photothermal therapy in extracellular Mtb and intracellular Mtb in macrophages. (A) Typical images of 7H11 plates for extracellular H37Ra upon Rif@Man-mPDA NPs and NIR irradiation treatment (808 nm, 1.2 w/cm², 5 min). (B) Statistical results for the effects of Rif@Man-mPDA NPs and NIR irradiation treatment (808 nm, 1.2 w/cm², 5 min) on the growth of extracellular H37Ra, n = 3,*$p < 0.05$, **$p < 0.01$, ***$p < 0.001$. (C) Typical images of 7H11 plates for intracellular H37Ra in THP-1 macrophages upon Rif@Man-mPDA NPs and NIR irradiation treatment (808 nm, 1.2 w/cm², 5 min). (D) Statistical results for the effects of Rif@Man-mPDA NPs and NIR irradiation treatment (808 nm, 1.2 w/cm², 5 min) on the growth of intracellular H37Ra in THP-1 macrophages, n = 3, *$p < 0.05$, **$p < 0.01$, ***$p < 0.001$.

3.5. Anti-TB effects of Rif@Man-mPDA NPs-mediated PTT on in vivo cutaneous tuberculosis mice model

Cutaneous Tuberculosis (CTB) remains one of the most dangerous public health issues that needs more effective control and treatment strategies. PTT has been highlighted as one of the most effective strategies for the treatment of skin-based diseases, suggesting its potential utility in combating CTB. Based on the *in vitro* and *ex vivo* anti-TB activities of Rif@Man-mPDA NPs-mediated PTT, it's necessary to further understand the *in vivo* anti-TB effects of this strategy for potential anti-TB application. Using H37Ra subcutaneously infected mice model (Fig. 6A), we applied Rif@Man-mPDA NPs-mediated PTT treatment and monitored the temperature changes upon PTT treatment. As shown in Fig. 6B and C, we found that the temperature at the skin site of Rif@Man-mPDA NPs treated mice increased rapidly during NIR irradiation in 5 min, which rapidly risen to 53.8 °C after 1 min, and then maintained at about 58 °C until the end of treatment. However, the temperature of saline or rifampicin upon PTT treatment didn't show any significant changes (Fig. 6B and C), which further indicated the excellent photothermal activity of Rif@Man-mPDA NPs *in vivo*. No significant changes in body weight were found in uninfected normal mice or H37Ra infected mice that were treated with Rif@Man-mPDA NPs or rifampicin drugs (Fig. 6D). But in H37Ra infected CTB mice, notable alleviation of skin pathological lesions was observed in mice treated with Rif@Man-

mPDA NPs and NIR irradiation, unlike other groups (Fig. 6E). We also analyzed the volume changes of cysts in the infection site, which indicated that Rif@Man-mPDA NPs-mediated PTT could significantly reduce the volume of cysts in the infection site of mice (Fig. 6F).

Then, by examining the CFU counts of H37Ra in the skin tissue lysates isolated from the infection sites, we observed significant reduction in the bacterial burden of H37Ra in mice treated with Rif@Man-mPDA NPs (Fig. 6G-H). Moreover, the bacterial burden of H37Ra was more significantly reduced in mice treated with Rif@Man-mPDA NPs with NIR irradiation compared with mice treated with Rif@Man-mPDA NPs alone. These results strongly suggested that Rif@Man-mPDA NPs-mediated PTT could significantly inhibit Mtb burdens in Mtb infected CTB model, which therefore show promising potentials for CTB treatments.

Next, to determine the degree of inflammation and ferroptosis at the site of Mtb infection, we analyzed skin sections by H&E staining. We found that the skin granulosum of infected mice was significantly thickened after H37Ra infection, as indicated by the green line in Fig. 7A. Moreover, after H37Ra infection, obvious inflammatory infiltration occurred in the subcutaneous tissue, as shown in blue box in Fig. 7A. In contrast, treatment with Rif@Man-mPDA NPs and NIR irradiation significantly reduced the inflammatory infiltration of skin tissue, and the thickness of the granulosum stratum was slightly restored to normal (Fig. 7A). Then, we further observed the changes of
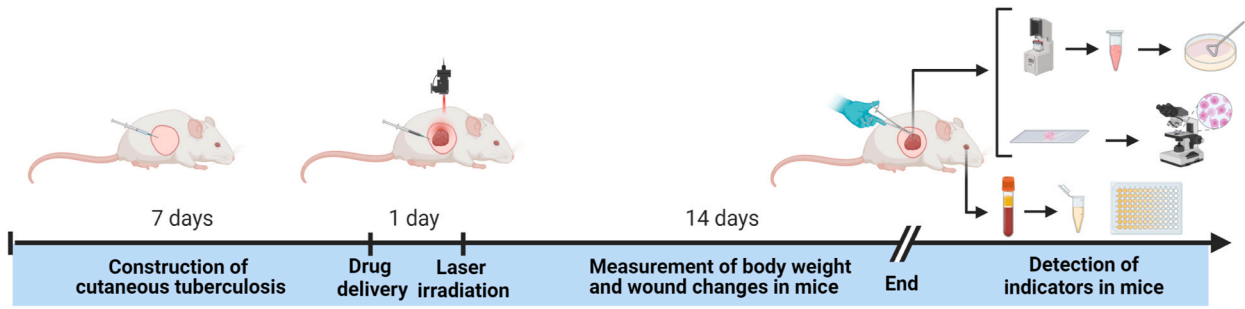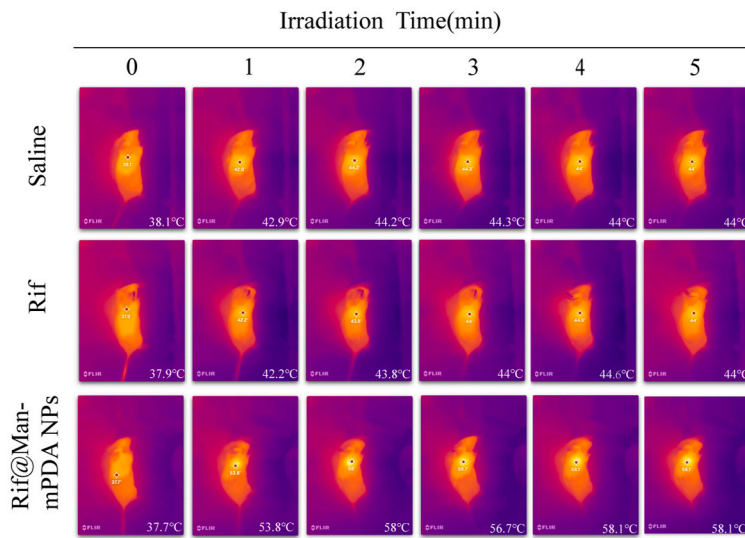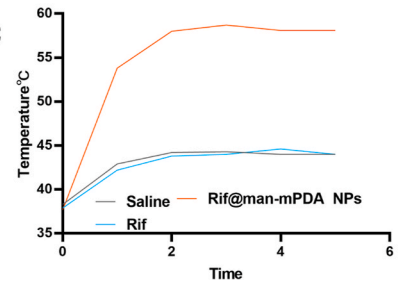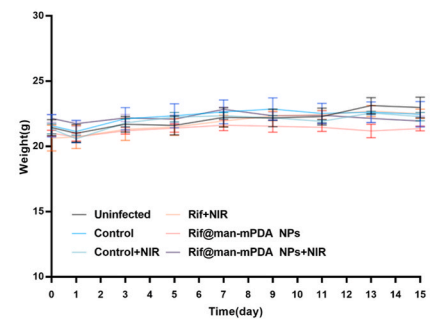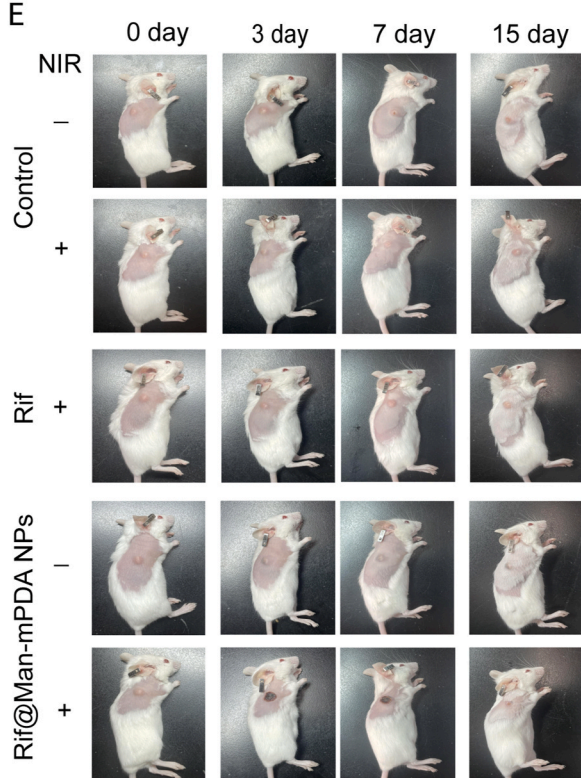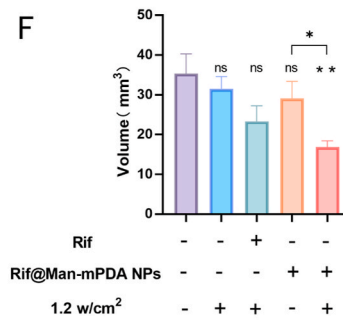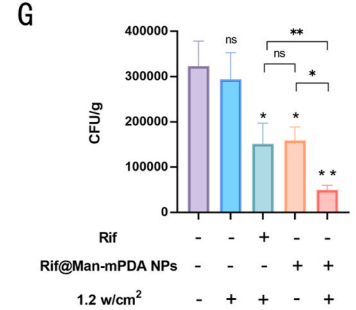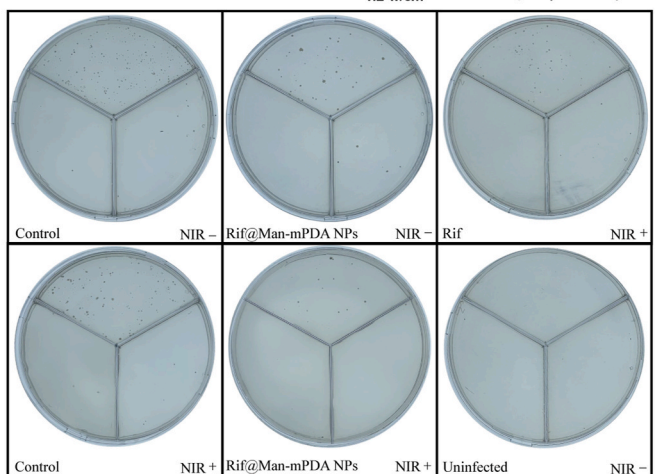
(caption on next page)

Fig. 6. In vivo anti-TB effects of Rif@Man-mPDA NPs-mediated photothermal therapy in Mtb infected mice. (A) Diagram for the mouse model of cutaneous tuberculosis and the experimental design of drug administration (Figure was created with Biorender.com) (B) Representative images of temperature changes in mice after saline, rifampicin, and Rif@Man-mPDA NPs administration and NIR irradiation (808 nm, 1.2 w/cm², 5 min) treatment. (C) Statistical results for the temperature changes in mice after saline, rifampicin, and Rif@Man-mPDA NPs administration and NIR irradiation (808 nm, 1.2 w/cm², 5 min) treatment. (D) Body weight changes of mice in different groups during the experiment, n = 6. (E) Typical pictures of skin granuloma in mice with different treatments during experiments. (F) Skin granuloma size at the endpoint of experiment in mice with different treatments, n = 6, *$p < 0.05$, **$p < 0.01$, ***$p < 0.001$. (G) Bacterial loads in the infected skin of mice with different treatments at the endpoint of experiment, n = 6, *$p < 0.05$, **$p < 0.01$, ***$p < 0.001$. (H) Typical 7H11 plates coated with lysate from the infected skin of mice with different treatments at the endpoint of experiment.
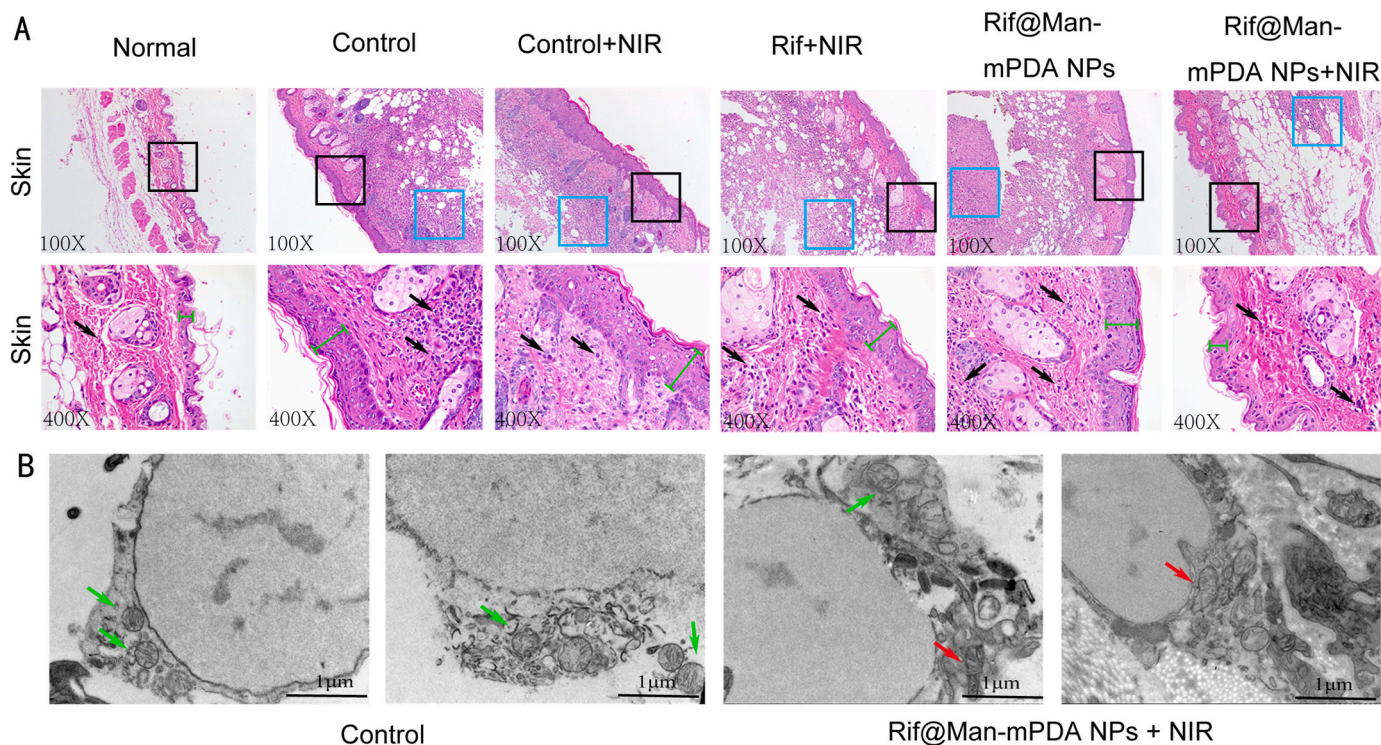

Fig. 7. Effects of Rif@Man-mPDA NPs-mediated photothermal therapy on the skin structures of mice. (A) Typical H&E staining images for the skin tissues of mice with different treatments. Blue boxes represent areas of pronounced inflammatory infiltration in the subcutis, specific leukocytes are indicted by black arrows and the green line segments represent the thickness of the granular layer in the skin of mice. (B) Typical TEM images for the skin tissues of mice with or without Rif@Man-mPDA NPs and NIR irradiation treatment, scale bar: 1 μm. (For interpretation of the references to colour in this figure legend, the reader is referred to the Web version of this article.)

mitochondria in the skin lesions by biological electron microscopy, and it was found that mitochondrial morphology was obviously changed with shrinkage and severe vacuolization appearance after H37Ra infection, while Rif@Man-mPDA NPs and NIR irradiation could significantly reverse these changes (Fig. 7B). These evidences further support the facts that Rif@Man-mPDA NPs-mediated PTT could not only reduces Mtb burdens *in vivo*, but could also alleviates the pathological damages induced by Mtb infection *in vivo*.

At last, we also determined whether Rif@Man-mPDA NPs-mediated PTT caused damage to other organs in infected mice, and made a preliminary assessment of the potential toxicity of this proposed anti-TB strategy. Firstly, Rif@Man-mPDA NPs-mediated PTT didn't produce any significant changes in the tissue structure of liver, spleen and kidney in the H37Ra infected mice (Fig. 8A–C). In addition, we also measured serum glutamic oxalic aminotransferase (AST), glutamic pyruvic aminotransferase (ALT) and blood urea nitrogen (BUN) as well as creatinine (CRE) as "hepatorenal function" parameters, similar with clinically routine tests for acute injury. The obtained results indicated that Rif@Man-mPDA NPs-mediated PTT didn't induce any significant changes in the AST, ALT, BUN and CRE levels (Fig. 8D–G), which further indicated that Rif@Man-mPDA NPs-mediated PTT treatment would not induce any significant changes of mice hepatorenal function *in vivo*.

Based on the above results, we propose a novel anti-TB strategy based on macrophage targeted Rif@Man-mPDA NPs system for photothermal therapy (PTT) against cutaneous tuberculosis (CTB) as shown in Fig. 9. These Rif@Man-mPDA NPs, directed by mannose receptors, are selectively internalized by macrophages and accumulate in lysosomes, releasing encapsulated rifampicin to eradicate intracellular Mtb. Rif@Man-mPDA NPs can effectively chelate intracellular Fe^{2+}, reduce lipid peroxidation and activate GPX4 of Mtb infected macrophages to inhibit ferroptosis of Mtb infected macrophages by Nrf2/HO-1 signaling pathway. Moreover, Rif@Man-mPDA NPs-mediated PTT could further increase the conversion of LC3B-I to LC3B-II and the formation of autophagosomes to promote autophagy of Mtb infected macrophages. And combing the modulation of ferroptosis and autophagy of Mtb infected macrophages, Rif@Man-mPDA NPs-mediated PTT could effectively kill intracellular Mtb *in vitro*, and further inhibit Mtb burdens in CTB mice model with alleviated pathology *in vivo*, which thus show promising potentials for clinical CTB treatment.

4. Conclusion

In this study, we developed an integrated therapeutic platform utilizing mannose-modified and rifampicin-loaded mesoporous polydopamine nanoparticles (Rif@Man-mPDA NPs) for treating cutaneous tuberculosis (CTB) by combining macrophage targeted drug delivery,
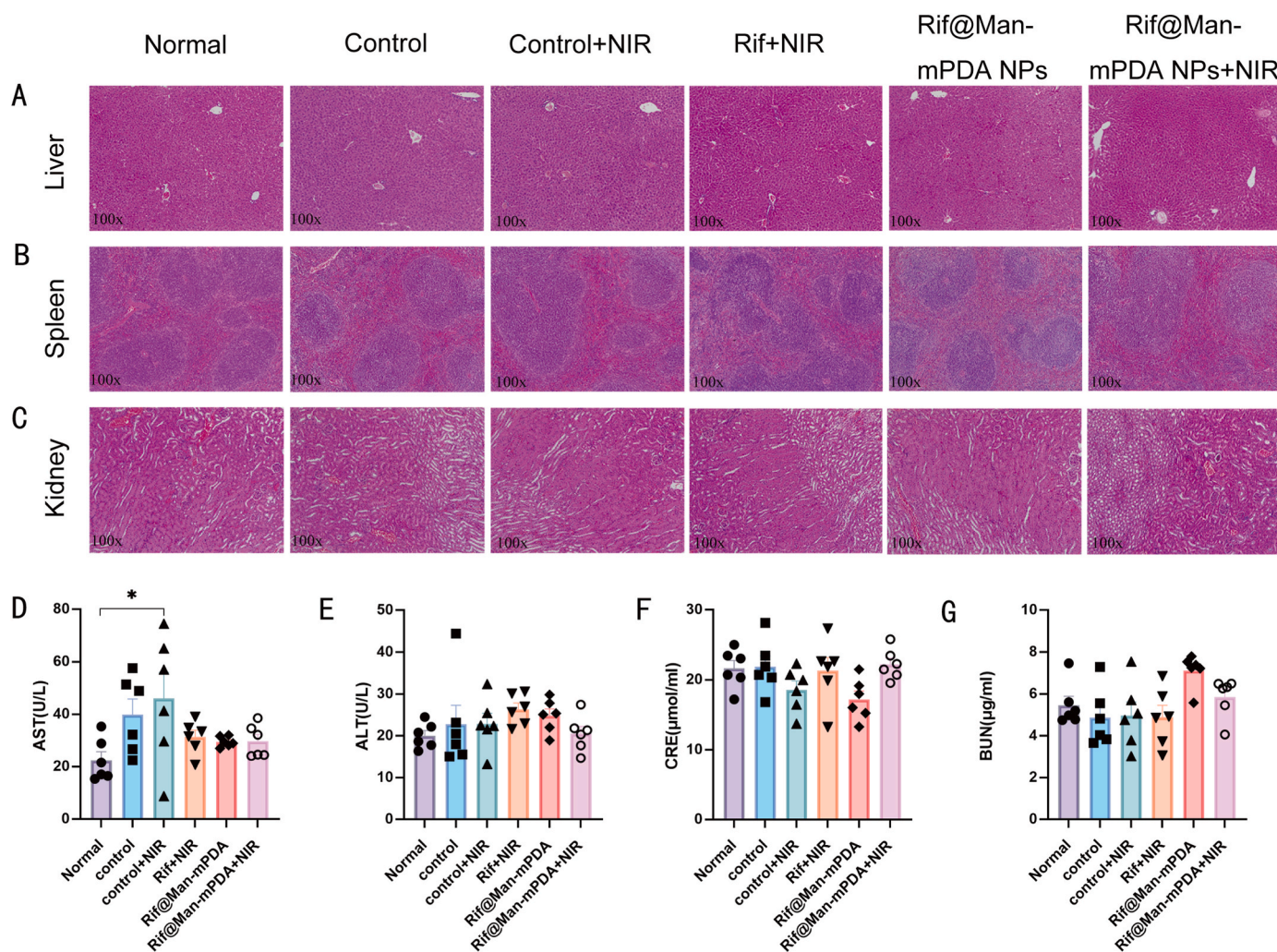
Fig. 8. Effects of Rif@Man-mPDA NPs-mediated photothermal therapy on mice tissue structure and "hepatorenal function" parameters of mice. (A) Typical H&E images of liver tissues in mice with different treatments. (B) Typical H&E images of spleen tissues in mice with different treatments. (C) Typical H&E images of kidney tissues in mice with different treatments. (D) Serum AST concentrations in mice with different treatments, n = 6, *$p < 0.05$, **$p < 0.01$, ***$p < 0.001$. (E) Serum ALT concentrations in mice with different treatments, n = 6. (F) Serum CRE concentrations in mice with different treatments, n = 6. (G) Serum BUN concentrations in mice with different treatments, n = 6.

photothermal therapy (PTT) and host immune clearance. The synthetized Rif@Man-mPDA NPs system was proved to show significant macrophage targeting effects with excellent photothermal properties. Rif@Man-mPDA NPs-mediated PTT could effectively inhibit immune escape mechanisms of Mtb by inhibiting ferroptosis in Mtb infected macrophages through chelating intracellular Fe^{2+}, inhibiting lipid peroxidation, increasing GPX4 expression and regulating Nrf2/HO-1 pathway. Moreover, Rif@Man-mPDA NPs-mediated PTT could further inhibit immune escape mechanisms of Mtb by effectively promoting autophagy of Mtb infected macrophages, which synergized the inhibition of ferroptosis of macrophages and macrophage targeted drug delivery for more effective intracellular Mtb clearance. This Rif@Man-mPDA NPs-mediated PTT could also effectively inhibit the Mtb burdens and alleviate the pathological lesions induced by Mtb infection without any systemic side effects in mouse CTB model. These results indicate that Rif@Man-mPDA NPs-mediated PTT can be used as a novel anti-TB strategy against CTB by synergizing macrophage targeted drug delivery and host cell immune defenses, which therefore show potential for the more effective treatment of CTB.

CRediT authorship contribution statement

Shuhao Fan: Writing – original draft, Software, Methodology, Funding acquisition, Formal analysis, Data curation. **Daina Zhao:** Writing – original draft, Funding acquisition, Formal analysis, Data curation. **Jiajun Wang:** Writing – original draft, Funding acquisition, Formal analysis, Data curation. **Yuhe Ma:** Funding acquisition. **Dongsheng Chen:** Funding acquisition. **Yuhe Huang:** Funding acquisition. **Tangxin Zhang:** Investigation, Funding acquisition. **Yilin Liu:** Formal analysis, Data curation. **Jiaojiao Xia:** Methodology. **Xueqin Huang:** Project administration, Methodology. **Yujia Lu:** Methodology. **Yongdui Ruan:** Software. **Jun-Fa Xu:** Writing – review & editing, Visualization. **Ling Shen:** Writing – review & editing, Visualization, Validation. **Fen Yang:** Writing – original draft, Visualization. **Jiang Pi:** Writing – review & editing, Writing – original draft, Data curation, Conceptualization.

Declaration of competing interest

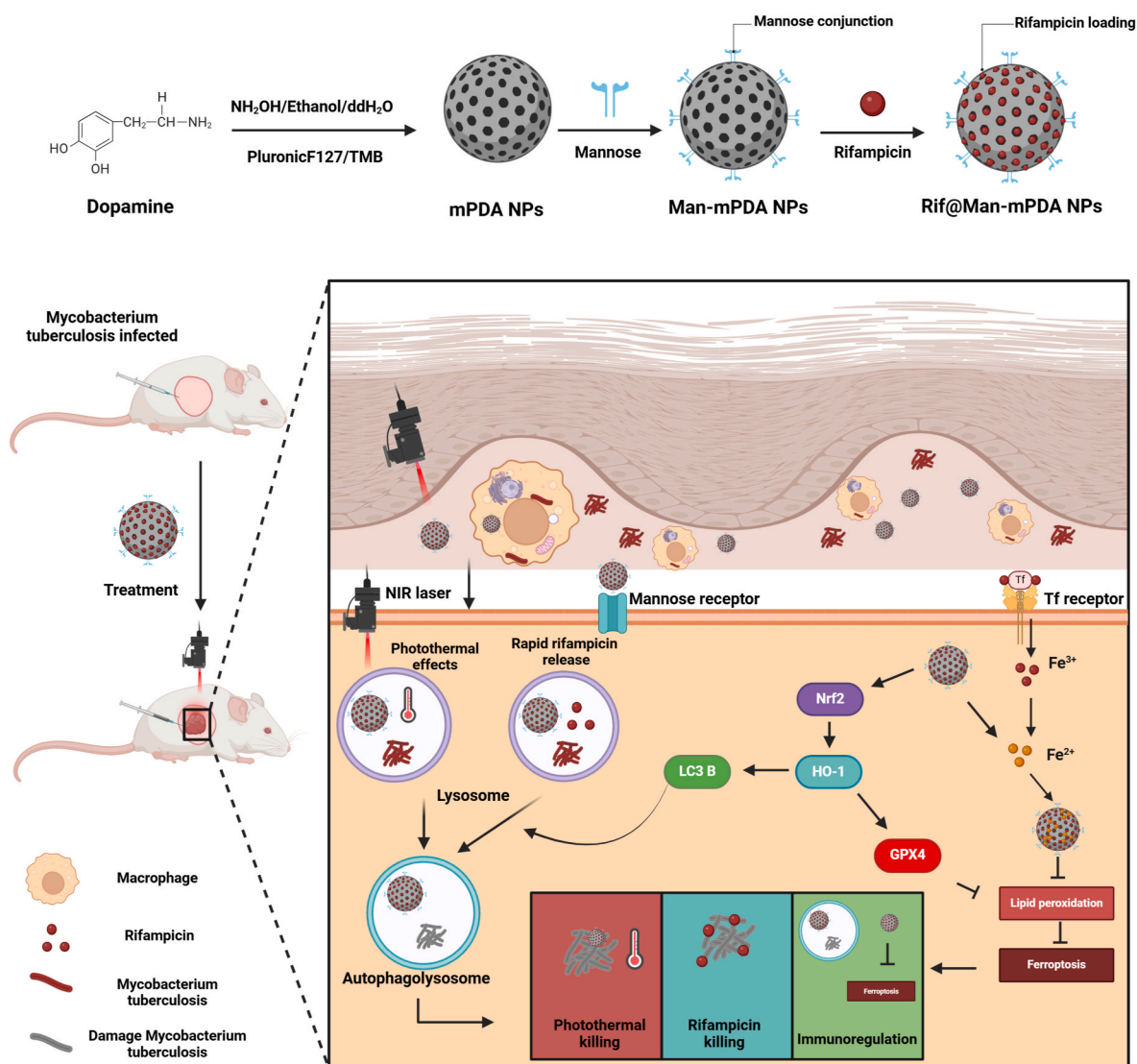The authors declare that they have no competing interests.

Fig. 9. Scheme for the preparation of Rif@Man-mPDA NPs and Rif@Man-mPDA NPs-mediated PTT for synergistic anti-TB treatment against cutaneous tuberculosis by combining PTT killing, host cell immune clearance and macrophage targeted drug delivery. (Figure was created with Biorender.com).

Data availability

Data will be made available on request.

Appendix A. Supplementary data

Supplementary data to this article can be found online at https://doi.org/10.1016/j.mtbio.2024.101232.

References

[1] WHO, Global Tuberculosis Report, 2023, Geneva : World Health Organization.pdf, 2023.

[2] S. Kaul, I. Kaur, S. Mehta, A. Singal, Cutaneous tuberculosis. Part I: pathogenesis, classification, and clinical features, J. Am. Acad. Dermatol. 89 (2023) 1091–1103, https://doi.org/10.1016/j.jaad.2021.12.063.

[3] Z. Hmama, S. Peña-Díaz, S. Joseph, Y. Av-Gay, Immunoevasion and immunosuppression of the macrophage by Mycobacterium tuberculosis, Immunol. Rev. 264 (2015) 220–232, https://doi.org/10.1111/imr.12268.

[4] Q. Chai, L. Wang, C.H. Liu, B. Ge, New insights into the evasion of host innate immunity by Mycobacterium tuberculosis, Cell. Mol. Immunol. 17 (2020) 901–913, https://doi.org/10.1038/s41423-020-0502-z.

[5] J. Barbagallo, P. Tager, R. Ingleton, R.J. Hirsch, J.M. Weinberg, Cutaneous tuberculosis: diagnosis and treatment, Am. J. Clin. Dermatol. 3 (2002) 319–328, https://doi.org/10.2165/00128071-200203050-00004.

[6] L.-W. Zhang, J. Wu, T. Chen, Papulonecrotic tuberculid, CMAJ (Can. Med. Assoc. J.) 196 (2024) E158, https://doi.org/10.1503/cmaj.231460.

[7] W. Zhai, F. Wu, Y. Zhang, Y. Fu, Z. Liu, The immune escape mechanisms of Mycobacterium tuberculosis, Int. J. Mol. Sci. 20 (2019) 340, https://doi.org/10.3390/ijms20020340.

[8] L. Qiang, Y. Zhang, Z. Lei, Z. Lu, S. Tan, P. Ge, Q. Chai, M. Zhao, X. Zhang, B. Li, Y. Pang, L. Zhang, C.H. Liu, J. Wang, A mycobacterial effector promotes ferroptosis-dependent pathogenicity and dissemination, Nat. Commun. 14 (2023) 1430, https://doi.org/10.1038/s41467-023-37148-x.

[9] Z. Cai, F. Xin, Z. Wei, M. Wu, X. Lin, X. Du, G. Chen, D. Zhang, Z. Zhang, X. Liu, C. Yao, Photodynamic therapy combined with antihypoxic signaling and CpG adjuvant as an in situ tumor vaccine based on metal-organic framework nanoparticles to boost cancer immunotherapy, Adv. Healthcare Mater. 9 (2020) e1900996, https://doi.org/10.1002/adhm.201900996.

[10] N. Tian, H. Duan, T. Cao, G. Dai, G. Sheng, H. Chu, Z. Sun, Macrophage-targeted nanoparticles mediate synergistic photodynamic therapy and immunotherapy of tuberculosis, RSC Adv. 13 (2023) 1727–1737, https://doi.org/10.1039/d2ra06334d.

[11] X. Huang, L. Chen, Y. Lin, K.I. Tou, H. Cai, H. Jin, W. Lin, J. Zhang, J. Cai, H. Zhou, J. Pi, Tumor targeting and penetrating biomimetic mesoporous polydopamine nanoparticles facilitate photothermal killing and autophagy blocking for synergistic tumor ablation, Acta Biomater. 136 (2021) 456–472, https://doi.org/10.1016/j.actbio.2021.09.030.

[12] D. Zhi, T. Yang, J. O'Hagan, S. Zhang, R.F. Donnelly, Photothermal therapy, J. Contr. Release 325 (2020) 52–71, https://doi.org/10.1016/j.jconrel.2020.06.032.

[13] Y. Yang, J. Zan, Y. Shuai, L. Yang, L. Zhang, H. Zhang, D. Wang, S. Peng, C. Shuai, In situ growth of a metal-organic framework on graphene oxide for the chemo-photothermal therapy of bacterial infection in bone repair, ACS Appl. Mater. Interfaces 14 (2022) 21996–22005, https://doi.org/10.1021/acsami.2c04841.

[14] S. Feng, J. Lu, K. Wang, D. Di, Z. Shi, Q. Zhao, S. Wang, Advances in smart mesoporous carbon nanoplatforms for photothermal–enhanced synergistic cancer therapy, Chem. Eng. J. 435 (2022) 134886, https://doi.org/10.1016/j.cej.2022.134886.

[15] H. Cheng, Y. He, J. Lu, Z. Yan, L. Song, Y. Mao, D. Di, Y. Gao, Q. Zhao, S. Wang, Degradable iron-rich mesoporous dopamine as a dual-glutathione depletion nanoplatform for photothermal-enhanced ferroptosis and chemodynamic therapy, J. Colloid Interface Sci. 639 (2023) 249–262, https://doi.org/10.1016/j.jcis.2023.02.041.

[16] Q. Xu, Y. Yang, J. Lu, Y. Lin, S. Feng, X. Luo, D. Di, S. Wang, Q. Zhao, Recent trends of mesoporous silica-based nanoplatforms for nanodynamic therapies, Coord. Chem. Rev. 469 (2022) 214687, https://doi.org/10.1016/j.ccr.2022.214687.

[17] K. Zhou, Z.-Z. Li, Z.-M. Cai, N.-N. Zhong, L.-M. Cao, F.-Y. Huo, B. Liu, Q.-J. Wu, L.-L. Bu, Nanotheranostics in cancer lymph node metastasis: the long road ahead, Pharmacol. Res. 198 (2023) 106989, https://doi.org/10.1016/j.phrs.2023.106989.

[18] F. Xie, M. Wang, Q. Chen, T. Chi, S. Zhu, P. Wei, Y. Yang, L. Zhang, X. Li, Z. Liao, Endogenous stimuli-responsive nanoparticles for cancer therapy: from bench to bedside, Pharmacol. Res. 186 (2022) 106522, https://doi.org/10.1016/j.phrs.2022.106522.

[19] S.L. Gaytan, E. Beaven, S.S. Gadad, M. Nurunnabi, Progress and prospect of nanotechnology for cardiac fibrosis treatment, Interdiscip Med 1 (2023) e20230018, https://doi.org/10.1002/INMD.20230018.

[20] F. Yang, Y. Lin, S. Shen, Y. Gu, C. Shuai, P. Feng, Polydopamine chelating strontium on graphene oxide enhances the mechanical and osteogenic induction properties of PLLA/PGA bone scaffold, International Journal of Bioprinting 10 (2024) 1829, https://doi.org/10.36922/ijb.1829.

[21] P. Feng, S. Peng, C. Shuai, C. Gao, W. Yang, S. Bin, A. Min, In situ generation of hydroxyapatite on biopolymer particles for fabrication of bone scaffolds owning bioactivity, ACS Appl. Mater. Interfaces 12 (2020) 46743–46755, https://doi.org/10.1021/acsami.0c13768.

[22] X. Cui, Q. Ruan, X. Zhuo, X. Xia, J. Hu, R. Fu, Y. Li, J. Wang, H. Xu, Photothermal nanomaterials: a powerful light-to-heat converter, Chem. Rev. 123 (2023) 6891–6952, https://doi.org/10.1021/acs.chemrev.3c00159.

[23] H. Wang, B. Li, Y. Sun, Q. Ma, Y. Feng, Y. Jia, W. Wang, M. Su, X. Liu, B. Shu, J. Zheng, S. Sang, Y. Yan, Y. Wu, Y. Zhang, Q. Gao, P. Li, J. Wang, F. Ma, X. Li, D. Yan, D. Wang, X. Zou, Y. Liao, NIR-II AIE luminogen-based erythrocyte-like nanoparticles with granuloma-targeting and self-oxygenation characteristics for combined phototherapy of tuberculosis, Adv. Mater. (2024) e2406143, https://doi.org/10.1002/adma.202406143.

[24] B. Li, W. Wang, L. Zhao, Y. Wu, X. Li, D. Yan, Q. Gao, Y. Yan, J. Zhang, Y. Feng, J. Zheng, B. Shu, J. Wang, H. Wang, L. He, Y. Zhang, M. Pan, D. Wang, B.Z. Tang, Y. Liao, Photothermal therapy of tuberculosis using targeting pre-activated macrophage membrane-coated nanoparticles, Nat. Nanotechnol. (2024), https://doi.org/10.1038/s41565-024-01618-0.

[25] Z. Zhou, Y. Yan, K. Hu, Y. Zou, Y. Li, R. Ma, Q. Zhang, Y. Cheng, Autophagy inhibition enabled efficient photothermal therapy at a mild temperature, Biomaterials 141 (2017) 116–124, https://doi.org/10.1016/j.biomaterials.2017.06.030.

[26] Cell membrane biomimetic nanomedicines for cancer phototherapy - Chen - 2023 - Interdisciplinary Medicine, Wiley Online Library 1 (2023) e20220012. https://onlinelibrary.wiley.com/doi/10.1002/INMD.20220012 (accessed March 1, 2024).

[27] W. Lin, S. Fan, K. Liao, Y. Huang, Y. Cong, J. Zhang, H. Jin, Y. Zhao, Y. Ruan, H. Lu, F. Yang, C. Wu, D. Zhao, Z. Fu, B. Zheng, J.-F. Xu, J. Pi, Engineering zinc oxide hybrid selenium nanoparticles for synergetic anti-tuberculosis treatment by combining Mycobacterium tuberculosis killings and host cell immunological inhibition, Front. Cell. Infect. Microbiol. 12 (2022) 1074533, https://doi.org/10.3389/fcimb.2022.1074533.

[28] Macrophage targeted iron oxide nanodecoys augment innate immunological and drug killings for more effective Mycobacterium Tuberculosis clearance, J. Nanobiotechnol. 21 (2023) 369. https://pubmed.ncbi.nlm.nih.gov/37817142/ (accessed January 20, 2024).

[29] C. Cui, K. Chakraborty, X.A. Tang, K.Q. Schoenfelt, A. Hoffman, A. Blank, B. McBeth, N. Pulliam, C.A. Reardon, S.A. Kulkarni, T. Vaisar, A. Ballabio, Y. Krishnan, L. Becker, A lysosome-targeted DNA nanodevice selectively targets macrophages to attenuate tumours, Nat. Nanotechnol. 16 (2021) 1394–1402, https://doi.org/10.1038/s41565-021-00988-z.

[30] Lysosome-targeted multifunctional lipid probes reveal the sterol transporter NPC1 as a sphingosine interactor, Proc. Natl. Acad. Sci. U. S. A. 120 (2023) e2213886120. https://pubmed.ncbi.nlm.nih.gov/36893262/ (accessed January 20, 2024).

[31] S. Ji, J. Li, X. Duan, J. Zhang, Y. Zhang, M. Song, S. Li, H. Chen, D. Ding, Targeted enrichment of enzyme-instructed assemblies in cancer cell lysosomes turns immunologically cold tumors hot, Angew Chem. Int. Ed. Engl. 60 (2021) 26994–27004, https://doi.org/10.1002/anie.202110512.

[32] H.-L. Luo, J. Pi, J.-A. Zhang, E.-Z. Yang, H. Xu, H. Luo, L. Shen, Y. Peng, G.-B. Liu, C.-M. Song, K.-Y. Li, X.-J. Wu, B.-Y. Zheng, H.-B. Shen, Z.W. Chen, J.-F. Xu, Circular RNA TRAPPC6B inhibits intracellular Mycobacterium tuberculosis growth while inducing autophagy in macrophages by targeting microRNA-874-3p, Clin Transl Immunology 10 (2021) e1254, https://doi.org/10.1002/cti2.1254.

[33] L. Shen, J. Frencher, D. Huang, W. Wang, E. Yang, C.Y. Chen, Z. Zhang, R. Wang, A. Qaqish, M.H. Larsen, H. Shen, S.A. Porcelli, W.R. Jacobs, Z.W. Chen, Immunization of Vγ2Vδ2 T cells programs sustained effector memory responses that control tuberculosis in nonhuman primates, Proc. Natl. Acad. Sci. U. S. A. 116 (2019) 6371–6378, https://doi.org/10.1073/pnas.1811380116.

[34] L. Chen, G. Zhang, G. Li, W. Wang, Z. Ge, Y. Yang, X. He, Z. Liu, Z. Zhang, Q. Mai, Y. Chen, Z. Chen, J. Pi, S. Yang, J. Cui, H. Liu, L. Shen, L. Zeng, L. Zhou, X. Chen, B. Ge, Z.W. Chen, G. Zeng, Ifnar gene variants influence gut microbial production of palmitoleic acid and host immune responses to tuberculosis, Nat. Metab. 4 (2022) 359–373, https://doi.org/10.1038/s42255-022-00547-3.

[35] Y. Wang, H. Zhong, X. Xie, C.Y. Chen, D. Huang, L. Shen, H. Zhang, Z.W. Chen, G. Zeng, Long noncoding RNA derived from CD244 signaling epigenetically controls CD8+ T-cell immune responses in tuberculosis infection, Proc. Natl. Acad. Sci. U. S. A. 112 (2015) E3883–E3892, https://doi.org/10.1073/pnas.1501662112.

[36] J. Pi, L. Shen, H. Shen, E. Yang, W. Wang, R. Wang, D. Huang, B.-S. Lee, C. Hu, C. Chen, H. Jin, J. Cai, G. Zeng, Z.W. Chen, Mannosylated graphene oxide as macrophage-targeted delivery system for enhanced intracellular M.tuberculosis killing efficiency, Mater. Sci. Eng., C 103 (2019) 109777, https://doi.org/10.1016/j.msec.2019.109777.

[37] J. Pi, Z. Zhang, E. Yang, L. Chen, L. Zeng, Y. Chen, R. Wang, D. Huang, S. Fan, W. Lin, H. Shen, J.-F. Xu, G. Zeng, L. Shen, Nanocages engineered from Bacillus Calmette-Guerin facilitate protective Vγ2Vδ2 T cell immunity against Mycobacterium tuberculosis infection, J. Nanobiotechnol. 20 (2022) 36, https://doi.org/10.1186/s12951-021-01234-3.

[38] X. Huang, H. Cai, H. Zhou, T. Li, H. Jin, C.E. Evans, J. Cai, J. Pi, Cobalt oxide nanoparticle-synergized protein degradation and phototherapy for enhanced anticancer therapeutics, Acta Biomater. 121 (2021) 605–620, https://doi.org/10.1016/j.actbio.2020.11.036.

[39] X. Huang, L. Chen, Y. Zhang, S. Zhou, H.-H. Cai, T. Li, H. Jin, J. Cai, H. Zhou, J. Pi, GE11 peptide conjugated liposomes for EGFR-targeted and chemophotothermal combined anticancer therapy, Bioinorgan. Chem. Appl. 2021 (2021) 5534870, https://doi.org/10.1155/2021/5534870.

[40] T.G.F. Souza, V.S.T. Ciminelli, N.D.S. Mohallem, A comparison of TEM and DLS methods to characterize size distribution of ceramic nanoparticles, J. Phys.: Conf. Ser. 733 (2016) 012039, https://doi.org/10.1088/1742-6596/733/1/012039.

[41] L. Zhang, P. Yang, R. Guo, J. Sun, R. Xie, W. Yang, Multifunctional mesoporous polydopamine with hydrophobic paclitaxel for photoacoustic imaging-guided chemo-photothermal synergistic therapy, Int. J. Nanomed. 14 (2019) 8647–8663, https://doi.org/10.2147/IJN.S218632.

[42] Nanoparticle size distribution quantification from transmission electron microscopy (TEM) of ruthenium tetroxide stained polymeric nanoparticles, J. Colloid Interface Sci. 604 (2021) 208–220, https://doi.org/10.1016/j.jcis.2021.04.081.

[43] W. She, K. Luo, C. Zhang, G. Wang, Y. Geng, L. Li, B. He, Z. Gu, The potential of self-assembled, pH-responsive nanoparticles of mPEGylated peptide dendron-doxorubicin conjugates for cancer therapy, Biomaterials 34 (2013) 1613–1623, https://doi.org/10.1016/j.biomaterials.2012.11.007.

[44] J. Lu, L. Song, S. Feng, K. Wang, Y. Mao, Y. Gao, Q. Zhao, S. Wang, Nanozyme-mediated biocatalysis as a mitochondrial oxidative stress amplifier for tumor nanocatalytic immunotherapy, Chem. Eng. J. 481 (2024) 148270, https://doi.org/10.1016/j.cej.2023.148270.

[45] A. Seth, H. Gholami Derami, P. Gupta, Z. Wang, P. Rathi, R. Gupta, T. Cao, J. J. Morrissey, S. Singamaneni, Polydopamine-mesoporous silica core-shell nanoparticles for combined photothermal immunotherapy, ACS Appl. Mater. Interfaces 12 (2020) 42499–42510, https://doi.org/10.1021/acsami.0c10781.

[46] L.Y.T. Chou, K. Ming, W.C.W. Chan, Strategies for the intracellular delivery of nanoparticles, Chem. Soc. Rev. 40 (2011) 233–245, https://doi.org/10.1039/c0cs00003e.

[47] F. Ahmad, A. Rani, A. Alam, S. Zarin, S. Pandey, H. Singh, S.E. Hasnain, N. Z. Ehtesham, Macrophage: a cell with many faces and functions in tuberculosis, Front. Immunol. 13 (2022) 747799, https://doi.org/10.3389/fimmu.2022.747799.

[48] M. Tang, B. Chen, H. Xia, M. Pan, R. Zhao, J. Zhou, Q. Yin, F. Wan, Y. Yan, C. Fu, L. Zhong, Q. Zhang, Y. Wang, pH-gated nanoparticles selectively regulate lysosomal function of tumour-associated macrophages for cancer immunotherapy, Nat. Commun. 14 (2023) 5888, https://doi.org/10.1038/s41467-023-41592-0.

[49] V.C. Korb, A.A. Chuturgoon, D. Moodley, Mycobacterium tuberculosis: manipulator of protective immunity, Int. J. Mol. Sci. 17 (2016) 131, https://doi.org/10.3390/ijms17030131.

[50] G. Xu, J. Wang, G.F. Gao, C.H. Liu, Insights into battles between Mycobacterium tuberculosis and macrophages, Protein Cell 5 (2014) 728–736, https://doi.org/10.1007/s13238-014-0077-5.

[51] A. Lam, R. Prabhu, C.M. Gross, L.A. Riesenberg, V. Singh, S. Aggarwal, Role of apoptosis and autophagy in tuberculosis, Am. J. Physiol. Lung Cell Mol. Physiol. 313 (2017) L218–L229, https://doi.org/10.1152/ajplung.00162.2017.

[52] A. Nisa, F.C. Kipper, D. Panigrahy, S. Tiwari, A. Kupz, S. Subbian, Different modalities of host cell death and their impact on Mycobacterium tuberculosis infection, Am. J. Physiol. Cell Physiol. 323 (2022) C1444–C1474, https://doi.org/10.1152/ajpcell.00246.2022.

[53] E.P. Amaral, C.L. Vinhaes, D. Oliveira-de-Souza, B. Nogueira, K.M. Akrami, B. B. Andrade, The interplay between systemic inflammation, oxidative stress, and tissue remodeling in tuberculosis, Antioxidants Redox Signal. 34 (2021) 471–485, https://doi.org/10.1089/ars.2020.8124.

[54] M.D. Shastri, S.D. Shukla, W.C. Chong, K. Dua, G.M. Peterson, R.P. Patel, P. M. Hansbro, R. Eri, R.F. O'Toole, Role of oxidative stress in the pathology and management of human tuberculosis, Oxid. Med. Cell. Longev. 2018 (2018) 7695364, https://doi.org/10.1155/2018/7695364.

[55] C. Ma, X. Wu, X. Zhang, X. Liu, G. Deng, Heme oxygenase-1 modulates ferroptosis by fine-tuning levels of intracellular iron and reactive oxygen species of macrophages in response to Bacillus Calmette-Guerin infection, Front. Cell. Infect. Microbiol. 12 (2022) 1004148, https://doi.org/10.3389/fcimb.2022.1004148.

[56] X. Shi, C. Li, L. Cheng, H. Ullah, S. Sha, J. Kang, X. Ma, Y. Ma, Mycobacterium tuberculosis Rv1324 protein contributes to mycobacterial persistence and causes pathological lung injury in mice by inducing ferroptosis, Microbiol. Spectr. 11 (2023) e0252622, https://doi.org/10.1128/spectrum.02526-22.

[57] C. Li, R. Stocker, Heme oxygenase and iron: from bacteria to humans, Redox Rep. 14 (2009) 95–101, https://doi.org/10.1179/135100009X392584.

[58] X. Yang, Y. Chen, J. Guo, J. Li, P. Zhang, H. Yang, K. Rong, T. Zhou, J. Fu, J. Zhao, Polydopamine nanoparticles targeting ferroptosis mitigate intervertebral disc degeneration via reactive oxygen species depletion, iron ions chelation, and GPX4 ubiquitination suppression, Adv. Sci. 10 (2023) e2207216, https://doi.org/10.1002/advs.202207216.

[59] L.-Y. Guo, Q.-S. Xia, J.-L. Qin, M. Yang, T.-Y. Yang, F.-T. You, Z.-H. Chen, B. Liu, H.-S. Peng, Skin-safe nanophotosensitizers with highly-controlled synthesized

[60] polydopamine shell for synergetic chemo-photodynamic therapy, J. Colloid Interface Sci. 616 (2022) 81–92, https://doi.org/10.1016/j.jcis.2022.02.046.

[60] H. Dong, Y. Xia, S. Jin, C. Xue, Y. Wang, R. Hu, H. Jiang, Nrf2 attenuates ferroptosis-mediated IIR-ALI by modulating TERT and SLC7A11, Cell Death Dis. 12 (2021) 1027, https://doi.org/10.1038/s41419-021-04307-1.

[61] O. Adedoyin, R. Boddu, A. Traylor, J.M. Lever, S. Bolisetty, J.F. George, A. Agarwal, Heme oxygenase-1 mitigates ferroptosis in renal proximal tubule cells, Am. J. Physiol. Ren. Physiol. 314 (2018) F702–F714, https://doi.org/10.1152/ajprenal.00044.2017.

[62] G.R. Golovkine, A.W. Roberts, H.M. Morrison, R. Rivera-Lugo, R.M. McCall, H. Nilsson, N.E. Garelis, T. Repasy, M. Cronce, J. Budzik, E. Van Dis, L.M. Popov, G. Mitchell, R. Zalpuri, D. Jorgens, J.S. Cox, Autophagy restricts Mycobacterium tuberculosis during acute infection in mice, Nat Microbiol 8 (2023) 819–832, https://doi.org/10.1038/s41564-023-01354-6.

[63] SIRT3 promotes antimycobacterial defenses by coordinating mitochondrial and autophagic functions, Authophagy 15 (2019) 1356–1375. https://pubmed.ncbi.nlm.nih.gov/30774023/ (accessed January 28, 2024).

[64] Y. Zhang, L. Zhang, J. Gao, L. Wen, Pro-death or pro-survival: contrasting paradigms on nanomaterial-induced autophagy and exploitations for cancer therapy, Acc. Chem. Res. 52 (2019) 3164–3176, https://doi.org/10.1021/acs.accounts.9b00397.

[65] X. Cai, S. Hua, J. Deng, Z. Du, D. Zhang, Z. Liu, N.U. Khan, M. Zhou, Z. Chen, Astaxanthin activated the Nrf2/HO-1 pathway to enhance autophagy and inhibit ferroptosis, ameliorating acetaminophen-induced liver injury, ACS Appl. Mater. Interfaces 14 (2022) 42887–42903, https://doi.org/10.1021/acsami.2c10506.

[66] X. Du, W. Wang, C. Wu, B. Jia, W. Li, L. Qiu, P. Jiang, J. Wang, Y.-Q. Li, Enzyme-responsive turn-on nanoprobes for in situ fluorescence imaging and localized photothermal treatment of multidrug-resistant bacterial infections, J. Mater. Chem. B 8 (2020) 7403–7412, https://doi.org/10.1039/d0tb00750a.

[67] Z. Liang, W. Liu, Z. Wang, P. Zheng, W. Liu, J. Zhao, Y. Zhong, Y. Zhang, J. Lin, W. Xue, S. Yu, Near-infrared laser-controlled nitric oxide-releasing gold nanostar/hollow polydopamine Janus nanoparticles for synergistic elimination of methicillin-resistant Staphylococcus aureus and wound healing, Acta Biomater. 143 (2022) 428–444, https://doi.org/10.1016/j.actbio.2022.02.029.

[68] M.A. Lake, K.N. Adams, F. Nie, E. Fowler, A.K. Verma, S. Dei, E. Teodori, D. R. Sherman, P.H. Edelstein, D.R. Spring, M. Troll, L. Ramakrishnan, The human proton pump inhibitors inhibit Mycobacterium tuberculosis rifampicin efflux and macrophage-induced rifampicin tolerance, Proc. Natl. Acad. Sci. U. S. A. 120 (2023) e2215512120, https://doi.org/10.1073/pnas.2215512120.

[69] G. Weiss, U.E. Schaible, Macrophage defense mechanisms against intracellular bacteria, Immunol. Rev. 264 (2015) 182–203, https://doi.org/10.1111/imr.12266.